Effects of Linearly Heated Left Wall on Natural Convection within a Superposed Cavity Filled with Composite Nanofluid-Porous Layers

Abstract

The effect of a linearly heated left sidewall on natural convection flows in a cavity filled with nanofluid-superposed porous layers is investigated numerically using the Galerkin finite element method. Two cases, which use the vertical and horizontal directions for the porous–nanofluid layers, are considered to investigate the natural convection in the flow inside a square enclosure. In both cases, the left wall is linearly heated, whereas the right wall is isothermally cooled. The horizontal walls are assumed to be thermally insulated. The Darcy–Brinkmann model is used to solve the governing equations in the porous layer. The results show that the nanofluid produces more enhancement of heat transfer compared to the base fluid. Increasing the Rayleigh number (Ra) values caused the intensity of the streamlines in case 2 to be stronger than that in case 1. Lower values of the thermal conductivity ratio (K_r) imply greater heat transfer enhancement than for the high thermal conductivity ratios. At the low values of the thermal conductivity ratio ($K_r < 1$) and Darcy number values ($Da < 10^{-3}$), the heat transfer is more enhanced for case 2 compared to case 1 while higher Darcy number produced case 1 overcome case 2.

Keywords: Natural convection; nonuniform heating; multilayers; nanofluid; porous medium.

1 Introduction

Convective heat transfer in a confined enclosure filled partly with a porous layer and partly with a fluid layer has received a great deal of attention from both the scientific and engineering communities due to its numerous applications, for instance heat exchangers, electronic cooling and solar collectors [1, 2]. These confined layers may be categorised as having vertical or horizontal orientations; additionally, the interface between the composite

layers may be permeable or impermeable. The selection of the model for the porous layers depends on the application type; however, due to the range of applications, the multilayer cavity (porous medium – fluid layers) in the vertical and the horizontal directions with a permeable interface has received increasing attention in the literature. The horizontal orientation of the porous media has been considered in publications that deal with free convection like [1]. The flow stability may be increased through the presence of a porous

Symbols	Name	Greek symbols	Name
Cp	specific heat capacity $(J.kg^{-1}K^{-1})$	α	thermal diffusivity $(m^2.s^{-1})$
Da	Darcy Number	β	thermal expansion coefficient (K^{-1})
g	gravitational field $(m.s^{-2})$	θ	dimensionless temperature
H	cavity Height (m)	μ	dynamic viscosity $(Pa.s)$
k	thermal conductivity $(W.m^{-1}K^{-1})$	ϑ	kinematic viscosity (m^2s^{-1})
K	permeability of porous medium (m^2)	ρ	Density $(kg.m^{-3})$
K_r	Thermal conductivity ratio $(\frac{K_p}{K_{nf}})$	ϕ	solid volume fraction
L	width of the enclosure (m)	ψ	stream function $(m^2.s^{-1})$
Nu	Nusselt number	Ψ	dimensionless stream function
Pr	Prandtl number	**Subscript**	
p	Pressure $(N.m^{-2})$	av	average
P	dimensionless pressure	bf	base fluid
Ra	Rayleigh number	c	cold
s	fluid layer thickness (m)	h	hot
S	dimensionless fluid layer thickness s/L	l	left
T	Temperature (K)	nf	nanofluid
u, v	velocity components in the x, y and z directions $(m.s^{-1})$	p	porous medium layer
U, V	dimensionless velocity components in the X and Y directions	r	right
x, y	Cartesian coordinates (m)	sp	solid nanoparticles
X, Y	dimensionless Cartesian coordinates		

medium. This situation also occurs when increasing the solid to fluid thermal conductivity ratio in the porous medium; however, increasing the Darcy number led to a reduced stability

envelope due to an increase in permeability. Thermal-driven flow in confined vertical porous-fluid layers has also received a great deal of attention in the scientific community. A considerable number of studies have been published on the two-dimensional natural convection that occurs in enclosures with deferentially heated vertical walls and adiabatically insulated horizontal walls where the porous layer is disposed vertically. Sathe, et al. [3] showed that increasing the porous layer thickness and the aspect ratio could minimize the heat transfer in the cavity if the fluid/solid (porous) thermal conductivity ratio is less than one. However, the effect of increasing the porous layer thickness on convective heat transfer could be also minimized by increasing the Darcy number.

Several methods have been used to control the flow and heat tranfer inside the enclosure. This includes the use of the lid-driven sidewall as reported in [4-6] or by using the effect of maganetic field as reported in [7-10] or by using fins as reported in [11]. In addition of using these controls, the use of nanoparticles with the base fluid can significantly enhance the physical properties of the base fluid and, therefore, improve the heat transfer characteristics [12-16]. This is because nanoparticles have a thermal conductivity that is higher than the base fluid. This important property of the nanofluid led to that the use of nanofluid in the convective flow within porous media has a wide range of practical engineering applications such as solar collectors, heat exchangers, material processing, heat preservation of thermal transport circuits, and the cooling of electrical units; these applications are listed in reference [17]. Furthermore, the use of a porous medium can improve convective heat transfer inside enclosures [1, 2]. A considerable number of studies [18-26] have been published on the effects of addition nanoparticles to the pure fluid. Hassan and Ismael [27] studied lid-driven square cavity effects on mixed convection within superposed nanofluid and porous layers. They concluded that the addition of nanoparticles led to a decrease in the rate of heat transfer when the Darcy number $\geq 10^{-4}$. Nguyen, et al. [28] completed a numerical investigation into the natural convection of

a Cu-water nanofluid in a non-Darcy, differentially heated porous cavity. The authors found that the addition of nanoparticles into the porous medium enhanced the rate of heat transfer, while the latter decreased or remained nearly constant through the porous region with increasing the nanofluid solid volume fraction at high and low values of both Rayleigh and Darcy numbers. Natural convection in a two-dimensional cavity arranged such that the layers lay vertically and were filled partly with porous medium and partly with Cu-water nanofluid was studied by Chamkha and Ismael [29]. The authors concluded that the convective heat transfer enhanced by using the nanofluid even with a low permeability porous medium, and that this decreased rapidly with increasing porous layer thickness. Alsabery, et al. [30] investigated the heatline visualization of natural convection in a trapezoidal cavity partly filled with a porous layer saturated with nanofluid and a non-Newtonian fluid layer. Some conclusions of this study suggested that the increased nanofluid thermal conductivity led to a rise in the circulation strength. It was also found that a higher value of the Nusselt number occurred at the volume fraction ϕ = 0.2; however, the Nusselt number dropped so that it was lower than other values of volume fraction ϕ = 0, 0.05 and 0.1 when the Darcy number was limited between 10^{-4} - 10^{-3}.

In addition to conventional uniform heating boundary conditions in natural convection enclosures, several studies have focussed in detail on non-uniformly heated wall thermal boundary conditions. This idea attracted researchers due to the fact that a heated wall may be subject to non-uniform thermal boundary conditions in a significant number of engineering applications, such as solar collector systems [31, 32], as well as the cooling of electronic components [32, 33] . This is due to the fact that non-uniform heating is likely to disguise or shade the heat transfer inside enclosures. Therefore, it is important to study the effect of non-uniform heated walls on convective heat transfer inside appropriate enclosures. There is an interested literature that focusses on the effects of non-uniform heating and magnetic field on

the convective heat transfer inside enclosures filled with a pure fluid like [34-37]. The effect of a linearly heated wall on the convective heat transfer in a square cavity filled with pure fluid has also been reported in the literature [38]. The influence of various thermal boundary conditions on the convective heat transfer in a cavity filled with a porous medium saturated with pure fluid has been reported [39-41] . Sathiyamoorthy, et al. [41] studied the influence of linear thermal boundary conditions on the natural convection inside a porous cavity. They observed that the rate of heat transfer oscillated at high Rayleigh and Darcy numbers due to the formation of secondary circulation. Wu [42] numerically examined the effects of sinusoidal heating applied to both vertical walls on natural convection in a porous rectangular enclosure using a thermal non-equilibrium model. They concluded that the rate of heat transfer in a porous enclosure can be enhanced by using sinusoidal heating. The effect of a magnetic field on fluid flow and heat transfer in a nanofluid-filled cavity with walls having sinusoidal temperature distribution was studied [43-46], while linearly heated vertical walls were examined in reference [47]. The influence of sinusoidal heating on the natural convection in a square cavity filled with nanofluid invesigated by [48, 49]. The study of natural convection in a square porous enclosure saturated with a nanofluid and partly heated from the bottom wall was numerically investigated by Bourantas, et al. [50]. They concluded that the rate of heat transfer is enhanced for different values of Rayleigh number in the presence of a porous medium, while there is no apparent sensitivity of the heat transfer to the presence or absence of a porous medium at low Rayleigh number. Sheremet and Pop [51] numerically examined the effect of sinusoidal heating on both sidewalls in a square porous enclosure saturated with nanofluid using Buongiorno's mathematical model. Recently, they also studied the use of the same model of natural convection in a wavy porous cavity with a sinusoidal temperature distribution on both sidewalls when the cavity is filled with a nanofluid. Very recently, Alsabery, et al. [52] studied the effect of inclination angle on the buoyancy-driven force inside an enclosure filled

partly with a porous medium and partly with a nanofluid and employing sinusoidal heating on the vertical walls using a finite difference methodology. The results showed that a higher enhancement was gained with a thin porous layer using Ag nanoparticles, whereas the use of Al_2O_3 enhanced heat transfer with increasing thickness of the porous layer. However, although the interested studies that mentioned above, a careful review of this literature reveals that there is a lack of fundamental information regarding the characteristics of the natural convection in a square enclosure filled by vertical or horizontal nanofluid-superposed porous layers with linear thermal boundary conditions on the left sidewall. The aim of the present study is to investigate the effects of linear heating of the left sidewall on the natural convection within an enclosure filled with nanofluid-superposed porous layers saturated with the same nanofluid.

2 Mathematical formulation and solution procedure

Natural convection is considered in a two-dimensional square enclosure with length *L,* filled by nanofluid-superposed porous layers in two cases, as shown schematically in Figure 1. Figure1 illustrates the first case considered in the study where the vertical porous layer is localized at the left-hand section of the cavity in the vertical direction, while in the second case the porous layer is localized at the bottom part of the cavity in the horizontal direction. The porous layer is saturated with a nanofluid and the remainder of the cavity is filled by the same nanofluid. The porous and nanofluid layers are simulated as having thicknesses S and $L - S$, respectively. In both cases considered in the present investigation, the left vertical wall of the cavity is assigned linearly heated boundary conditions, while the right vertical wall is isothermally cooled; the top and bottom walls are thermally insulated. The interface between the nanofluid layer and porous layer is proposed to be permeable, while all outer boundaries are assumed to be impermeable. The nanofluid is composed of water-based fluid containing Cu nanoparticles. The thermophysical properties of the nanofluid are illustrated in Table 1. The

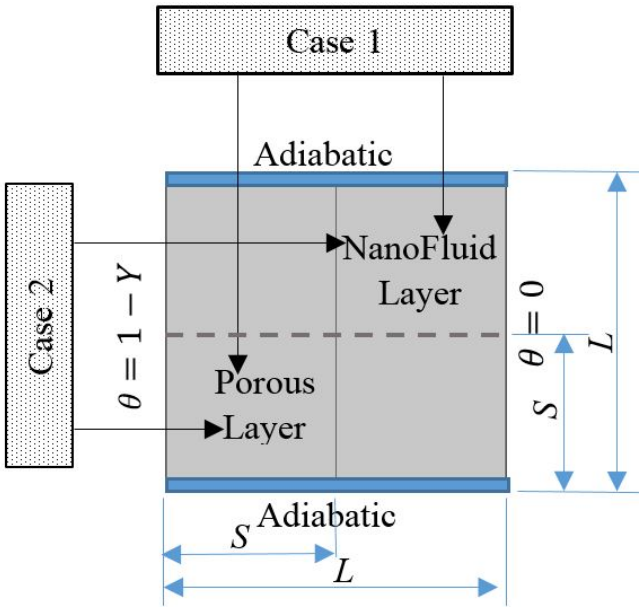

Figure 1: Physical domain of vertical (case 1) and horizontal (case 2) directions of the composite nanofluid-porous medium layers.

base fluid and nanoparticles are taken to form a homogeneous mixture and thermally equilibrium with no slip condition occurs between them. In addition, a thermal equilibrium between the solid matrix of the porous medium and the nanofluid is assumed. The flow is considered to be steady, laminar, and incompressible with constant physical properties except for the density, where the latter is assumed to vary with temperature according to the Boussinesq approximation.

Table 1: Thermo-physical properties of water and Cu nanoparticles [29].

Physical properties	***Cp* (J/Kg. k)**	**ρ (kg/m^3)**	***k* (W. m^{-1}K^{-1})**	**β *10^{-5} (1/K)**
Water	4179	997.1	0.613	21
Cu	385	8933	401	1.67

The convective heat transfer was simulated using a Navier-Stokes model for the nanofluid layer while the Darcy–Brinkman model is invoked to model the porous layer. Based on these assumptions, the dimensionless governing equations of the nanofluid and porous layers can be written as follows:

The dimensionless governing equations for the nanofluid layer are [14]:

$$\frac{\partial U_{nf}}{\partial X}+\frac{\partial V_{nf}}{\partial Y}=0 \tag{1}$$

$$U_{nf}\frac{\partial U_{nf}}{\partial X}+V_{nf}\frac{\partial U_{nf}}{\partial Y}=-\frac{\partial P}{\partial X}+\frac{\rho_f}{\rho_{nf(1-\phi)^{2.5}}}\left(\frac{\partial^2 U_{nf}}{\partial X^2}+\frac{\partial^2 U_{nf}}{\partial Y^2}\right) \tag{2}$$

$$U_{nf}\frac{\partial V_{nf}}{\partial X}+V_{nf}\frac{\partial V_{nf}}{\partial Y}=-\frac{\partial P}{\partial Y}+\frac{\rho_f}{\rho_{nf(1-\phi)^{2.5}}}\left(\frac{\partial^2 V_{nf}}{\partial X^2}+\frac{\partial^2 V_{nf}}{\partial Y^2}\right)+\frac{(\rho\beta)_{nf}}{\rho_{nf}\,\beta_{bf}}*Pr.Ra.\theta_{nf} \tag{3}$$

$$U_{nf}\frac{\partial \theta_{nf}}{\partial X}+V_{nf}\frac{\partial \theta_{nf}}{\partial Y}=\frac{\alpha_{nf}}{\alpha_{bf}}\left(\frac{\partial^2 \theta_{nf}}{\partial X^2}+\frac{\partial^2 \theta_{nf}}{\partial Y^2}\right) \tag{4}$$

On the other hand, the dimensionless governing equations for the porous layer are:

$$\frac{\partial U_p}{\partial X}+\frac{\partial V_p}{\partial Y}=0 \tag{5}$$

$$U_p\frac{\partial U_p}{\partial X}+V_p\frac{\partial U_p}{\partial Y}=-\frac{\partial P}{\partial X}+\frac{\rho_f}{\rho_{nf(1-\phi)^{2.5}}}\left(\frac{\partial^2 U_p}{\partial X^2}+\frac{\partial^2 U_p}{\partial Y^2}\right)-\frac{\rho_f}{\rho_{nf(1-\phi)^{2.5}}}\frac{Pr}{Da}\,U_p \tag{6}$$

$$\begin{aligned} U_p\frac{\partial V_p}{\partial X}+V_p\frac{\partial V_p}{\partial Y} &= -\frac{\partial P}{\partial Y}+\frac{\rho_f}{\rho_{nf(1-\phi)^{2.5}}}\left(\frac{\partial^2 V_p}{\partial X^2}+\frac{\partial^2 V_p}{\partial Y^2}\right)+\frac{(\rho\beta)_{nf}}{\rho_{nf}\,\beta_{bf}}*Pr.Ra.\theta_p \\ &\quad -\frac{\rho_f}{\rho_{nf(1-\phi)^{2.5}}}\frac{Pr}{Da}\,V_p \end{aligned} \tag{7}$$

$$U_{nf}\frac{\partial \theta_{nf}}{\partial X}+V_{nf}\frac{\partial \theta_{nf}}{\partial Y}=\frac{\alpha_{eff}}{\alpha_{bf}}*\left(\frac{\partial^2 \theta}{\partial X^2}+\frac{\partial^2 \theta}{\partial Y^2}\right) \tag{8}$$

The dimensionless dependent and independent variables and parameters are as follows:

$$\begin{aligned} &X=\frac{x}{L},\ Y=\frac{y}{L},\ U=\frac{uL}{\alpha_{bf}},\ V=\frac{vL}{\alpha_{bf}},\ P=\frac{PL}{\rho_{bf}\alpha_{bf}^2},\ \theta_{nf}=\frac{T_{nf}-T_c}{T_h-T_c},\ \theta_p=\frac{T_p-T_c}{T_h-T_c}, \\ &Ra=\frac{\beta_{bf}.g.\Delta T.L^3}{\vartheta_{bf}.\alpha_{bf}},\ Pr=\vartheta_{bf}/\alpha_{bf},\ Da=\frac{K}{L^2} \end{aligned} \tag{9}$$

These relations are combined with the adopted relations that prescribe the physical properties of the nanofluid that are considered to depend on the nanoparticles' volume fraction, ϕ, as follows [53]:

$$\rho_{nf} = (1-\phi)\rho_{bf} + \phi\rho_{np} \tag{10}$$

$$\mu_{nf} = \frac{\mu_{bf}}{(1-\phi)^{2.5}} \tag{11}$$

$$(\rho Cp)_{nf} = (1-\phi)(\rho Cp)_{bf} + \phi(\rho Cp)_{np} \tag{12}$$

$$\beta_{nf} = (1-\phi)(\rho\beta)_{nf} + \phi(\rho\beta)_{np} \tag{13}$$

$$(\rho\beta)_{nf} = (1-\phi)\rho_{bf} + \phi\rho_{np} \tag{14}$$

$$k_{nf} = \frac{\left(k_{np} + 2k_{bf}\right) - 2\phi\left(k_{bf} - k_{np}\right)}{\left(k_{np} + 2k_{bf}\right) + \phi\left(k_{bf} - k_{np}\right)} k_{bf} \tag{15}$$

$$K_{eff} = K_r * \frac{k_{nf}}{k_{bf}} \tag{16}$$

where K_r is the porous/nanofluid thermal conductivity ratio, K_{eff} is the effective thermal conductivity, and

$$\alpha_{nf} = \frac{k_{nf}}{(\rho Cp)_{nf}}, \tag{17}$$

$$\alpha_{eff} = \frac{k_{eff}}{(\rho Cp)_{nf}} \tag{18}$$

The boundary conditions for each case (vertical and horizontal orientation of the porous medium –nanofluid layers) are:

At the left hot wall $U=0,\ V=0,\ \theta = 1 - Y$

At the right cold wall $U=0,\ V=0,\ \theta = 0$

At the top and bottom insulated walls $U=0,\ V=0,\ \frac{\partial\theta}{\partial Y} = 0$ (19)

The interface boundary conditions of the nanofluid-porous medium layers are assumed permeable with equally values of tangential and normal velocities, shear and normal stresses and temperature which can be written as:

$$\mu_P = \mu_{nf}, \quad \theta_p = \theta_{nf}, \quad \psi_p = \psi_{nf} \tag{20}$$

$$\frac{\partial \theta_{nf}}{\partial X} = K_r \frac{\partial \theta_p}{\partial X} \tag{21}$$

where K_r is the ratio of the effective thermal conductivity of the porous medium to the thermal conductivity of the nanofluid.

2.1 Stream function and Nusselt number

2.1.1 *Stream function*

The fluid motion within the porous medium-nanofluid layers can be simulated using the stream function Ψ produced from the velocity components $U$and V [40]where,

$$U = \frac{\partial \Psi}{\partial Y}, \quad V = -\frac{\partial \Psi}{\partial X} \tag{22}$$

These relations of the velocity components for two dimensional flows yield to a single equation as follows

$$\frac{\partial^2 \Psi}{\partial X^2} + \frac{\partial^2 \Psi}{\partial Y^2} = \frac{\partial U}{\partial Y} - \frac{\partial V}{\partial X} \tag{23}$$

According to this equation, the positive sign of Ψ represents the flow in the counter-clockwise direction while the negative sign denotes the clockwise direction.

2.1.2 *Nusselt number*

Along the left heated wall, the local and average Nusselt numbers are defined by the following relations [29]:

$$Nu = -\frac{k_{nf}}{k_f}\frac{\partial \theta}{\partial n} \tag{24}$$

where n refers to the normal direction on a plane.

$$Nu_l = \frac{k_{nf}}{k_f}\left(\frac{\partial \theta_p}{\partial X}\right)_{X=0} \tag{25}$$

$$Nu_r = \frac{k_{nf}}{k_f}\left(\frac{\partial \theta_{nf}}{\partial X}\right)_{X=1} \tag{26}$$

$$Nu_{av} = \int_0^1 Nu_l \, dY \tag{27}$$

3 Numerical solution

The Galerkin Finite Element Method (GFEM) is used to solve the dimensionless governing equations (2.1-2.8) with the boundary conditions for the assumed problem using the Computational Fluid Dynamics (CFD) solver in the COMSOL 5.1 software suite. The SIMPLE algorithm [54] was used to couple the continuity and momentum equations. The nonlinear residual equations were solved using the Galerkin finite element method, where the velocity components (U, V), and temperature θ are subjected to the basis set as illustrated in [55]. To evaluate the integrals of these equations, three-point Gaussian quadrature is used. In addition, the Newton-Raphson method is used to evaluate the expansion coefficients of the non-linear residual equations.

The iteration is terminated when the dependent variables reach steady state and satisfy the criterion:

$$\frac{\sum_{i=1}^{m}\sum_{j=1}^{n}\left|\Phi_{i,j}^{r+1}-\Phi_{i,j}^{r}\right|}{\sum_{i=1}^{m}\sum_{j=1}^{n}\left|\Phi_{i,j}^{r+1}\right|} \leq 10^{-6} \tag{3.1}$$

where Φ represents the velocity components (U, V), temperature θ, or the pressure in the domain. The subscripts i and j indicate the i^{th} and j^{th} grid in the x and y directions, respectively. The superscript r refers to the rth iteration. m and n represent the total number of nodes. The biquadratic quadrilateral element is used in the present study to discretize the solution domain. This element has nine nodes, four of which are located at the vertices and one more is centred between every two vortices as well as at the centre of the element.

3.1 Code Validation

The present study is validated by comparing its predictions with the results determined by Chamkha and Ismael [29]. The validation test case domain is that of a two-dimensional laminar flow for steady natural convection inside an enclosure superposed in a vertical direction by the nanofluid and porous layers, which are filled partly with nanofluid and partly with a porous medium saturated with the same nanofluid, as shown in Figure 2. The vertical walls of the cavity consisted of two opposing isothermal boundary conditions while the

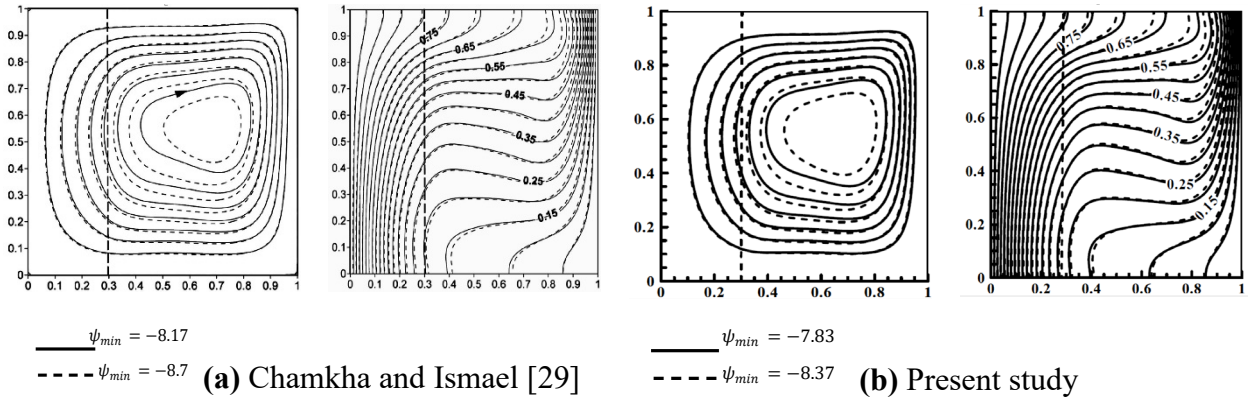

Figure 2: Streamlines (left) and isotherms (right), for a square cavity with uniform hot left sidewall and cold right sidewall and adiabatic top and bottom walls at Ra = 10^5, Da =10^{-5}, aspect ratio=1, porous layer thickness=0.3, ϕ = **0** (solid lines) and ϕ = **0.05** (dashed lines). The left panel corresponds to (a) Chamkha and Ismael [29] and the right panel corresponds to (b) the present study.

horizontal walls were kept insulated. The results of the comparison of the stream function and isotherms are investigated for $Ra = 10^5$, $Da = 10^{-5}$, aspect ratio = 1 and a porous layer thickness equal to 0.3. The nanofluid is composed of water as a base fluid and copper nanoparticles at a volume fraction ϕ of 0.05. In addition, Figure 3 shows a comparison between the results of this study and those was presented by Sathiyamoorthy, et al. [41]. The cavity was entirely filled with a porous medium saturated by air with linearly and uniformly heated left and bottom walls, whilst the right wall was uniformly cold and the upper wall was kept isolated. The selected parameters of the comparison were $Ra = 10^6$, $Da = 10^{-3}$ and $Pr = 0.7$. The Brinkman-extended Darcy model was used to solve the equations governing the fluid flow in the porous media for each of the selected comparisons. The results can be seen to be in a good agreement, and give further confidence as to the accuracy of the currently selected FEM solver.6

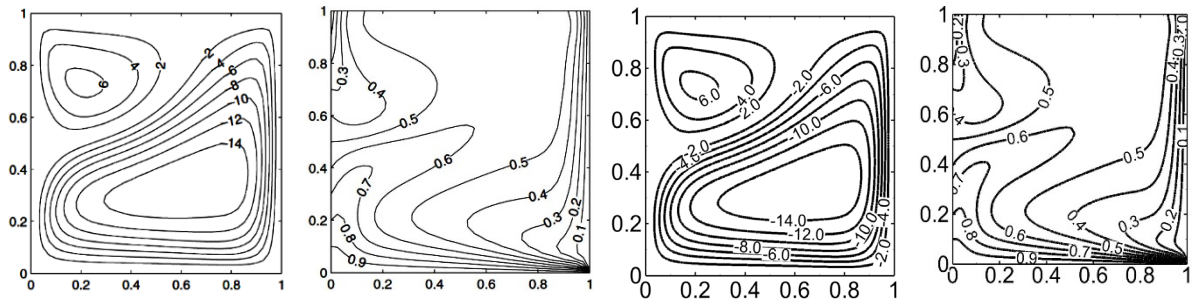

(a) Sathiyamoorthy, et al. [41] **(b)** Present study

Figure 3: Streamlines (left) and isotherms (right), for the case θ = 1-y on the left wall and θ = 0 on the right wall and adiabatic top and bottom walls at $Ra = 10^6$, $Da = 10^{-5}$ and Pr = 0.7. The left panel corresponds to **(a)** Sathiyamoorthy, et al. [41] and the right panel corresponds to **(b)** the present study.

To increase confidence in the results produced by this program, Figure 4 shows a further validation with the numerical and experimental results that were presented by Beckermann, et al. [56] for the natural convection inside superposed enclosure with pure fluid - porous medium layers. The validation is examined for the Brinkman-Forchheimer with Darcy extended model for experiment 2 by using the water as a working fluid in the layers. A considerable difference between the numerical and the experimental results attributed to the inaccuracies in

determining of the exact position of the thermocouple probe and the non-uniformities of the porosity at the walls. The average percentage of the discrepancies between the experimental and numerical solution is about 7%, however; the comparison of the present results showed good agreement between our results and those reported in the literature.

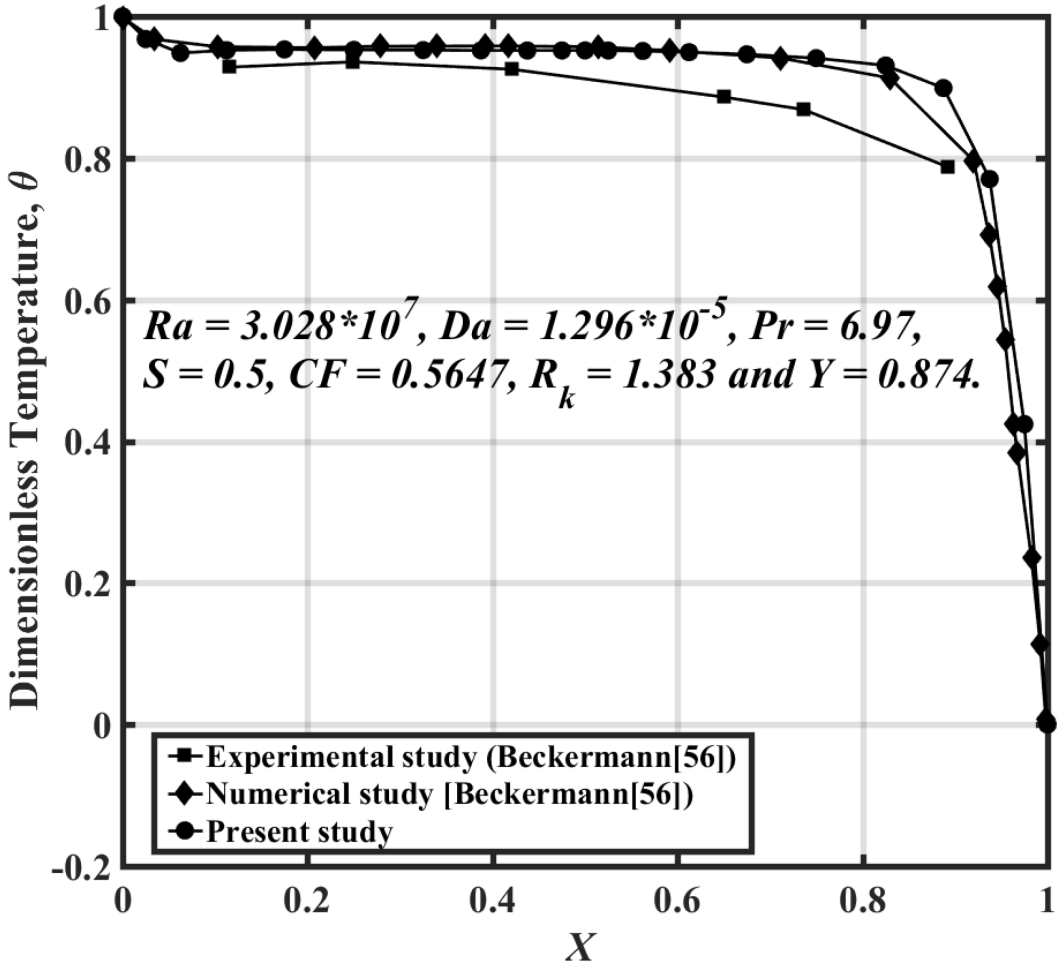

Figure 4: Validation of numerical and experimental results presented by Beckermann, et al. [56] with the present result.

3.2 Grid Independence Test

Several independent grid tests were performed with the grid sizes of 6400, 10,000, 14,400, 16,900, 19,600 and 25,600 to determine the proper size of this study. Figure 5 illustrates the calculated average Nusselt number at different grid sizes for an enclosure partly filled with nanofluid and partly filled with a porous layer saturated with the same nanofluid for

cases 1 and 2, where $Ra = 10^7$, $Da = 10^{-3}$, $K_r = 1$, $\phi = 0.1$ and $S = 0.3$. A grid size of 16,900 was used to assess the analysis cost and the accuracy and of the numerical procedure due to obtaining the convergence solution values of the average Nusselt number that started at this value for the grid testing.

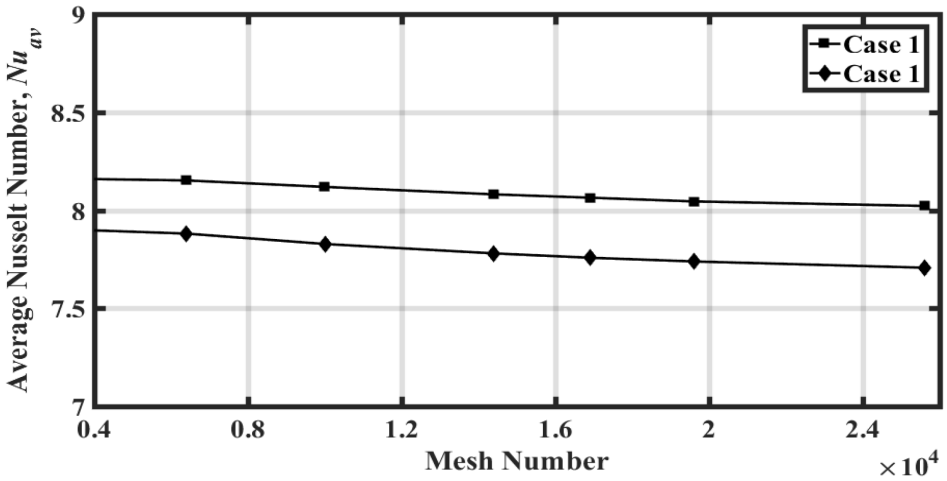

Figure 5: Grid testing for the average Nusselt number at different mesh numbers

4 Results and discussion

Two cases of the vertical and horizontal directions of porous–nanofluid layers are considered to investigate the natural convection of the flow inside a square enclosure. Case 1 and case 2 deal with vertical and horizontal porous-nanofluid layers, respectively. The current work shows the characteristics of the numerical results for the contours of the streamlines and isotherms, as well as selected profiles for the velocity components (U, V, R) and temperature at the interface between the porous and nanofluid layers. In addition, the local Nusselt number on the left and right walls and the average Nusselt number on the left heated wall are presented graphically for different dimensionless parameters. The selected parameters that affect flow and heat transfer are $Ra = 10^3$ - 10^7, $Da = 10^{-7}$ - 10^{-1}, $\phi = 0.1$ and $K_r = 0.1$ - 100. A detailed discussion of the heat transport based on natural convection for the two cases is presented in the following sections.

4.1 Streamlines and isotherms

4.1.1 *Vertical porous-nanofluid layers (case 1)*

Figure 6 illustrates the contours for the streamlines (upper row) and isotherms (lower row) that depict the numerical results for different effects of dimensionless parameters such as S, Ra, Da, and K_r when the porous and nanofluid layers lie in a vertical direction (case 1). Figure 6(a-c) illustrates the effect of the porous layer thickness (S) on the flow behaviour and temperature distribution inside the cavity for Ra = 10^6, Da = 10^{-3}, and K_r = 1. Due to the application of linear heating to the left wall and uniform cooling across the right wall, the nanofluid inside the porous layer rises along the left sidewall and flows down along the cooled right wall in the nanofluid layer, forming two circulations. One of these, as the main vortex, covered most of the cavity in a clockwise direction while the secondary circulation appears at the top left corner of the cavity and moves in an anticlockwise direction. For all values of S, the addition of 10% of copper nanoparticles to the pure fluid (water) causes the streamlines' strength for the main cell to be stronger than the pure fluid. This is because the nanofluid has the ability to absorb more thermal energy than the pure fluid. This gives an indication that the addition of nanoparticles to the pure fluid contributes to an increase in various physical properties such as the density, viscosity and thermal conductivity of the nanofluid, as shown in equations (10), (11) and (15). It is interesting to note that as the value of S increases, the centre of the main cell moves from a location close to the interface line towards the right cold wall.Another interesting point that may be noted in Figure 6(a-c) is that the streamlines for porous layers with low thicknesses are more effective than thick porous layers. This can be clearly seen from the stream function values, $|\Psi_{min}|$, where for S = 0.1, 0.3 and 0.5, the percentage gain of $|\Psi_{min}|$ values are 13%, 7.9% and 6.7%, respectively. The effects of increasing porous layer thickness on the reduction of circulation strength are attributed to the hydrodynamic resistance provided by the porous layer. The isotherm lines are parallel to the

cold right-hand wall, whereas they cross the left-hand heated wall. The temperature contour with $\theta = 0.31$ was pushed towards the upper left corner of the cavity, which gradually became denser at $S = 0.1$, and more so than at S values of 0.3 and 0.5. The vertical pattern of the majority of the isotherm lines within the porous layer indicates the dominance of conduction as the mechanism of heat transfer, whereas the horizontal isotherm pattern indicates convective heat transfer within the nanofluid layer. It is interesting to note that the spot produces by the isotherm

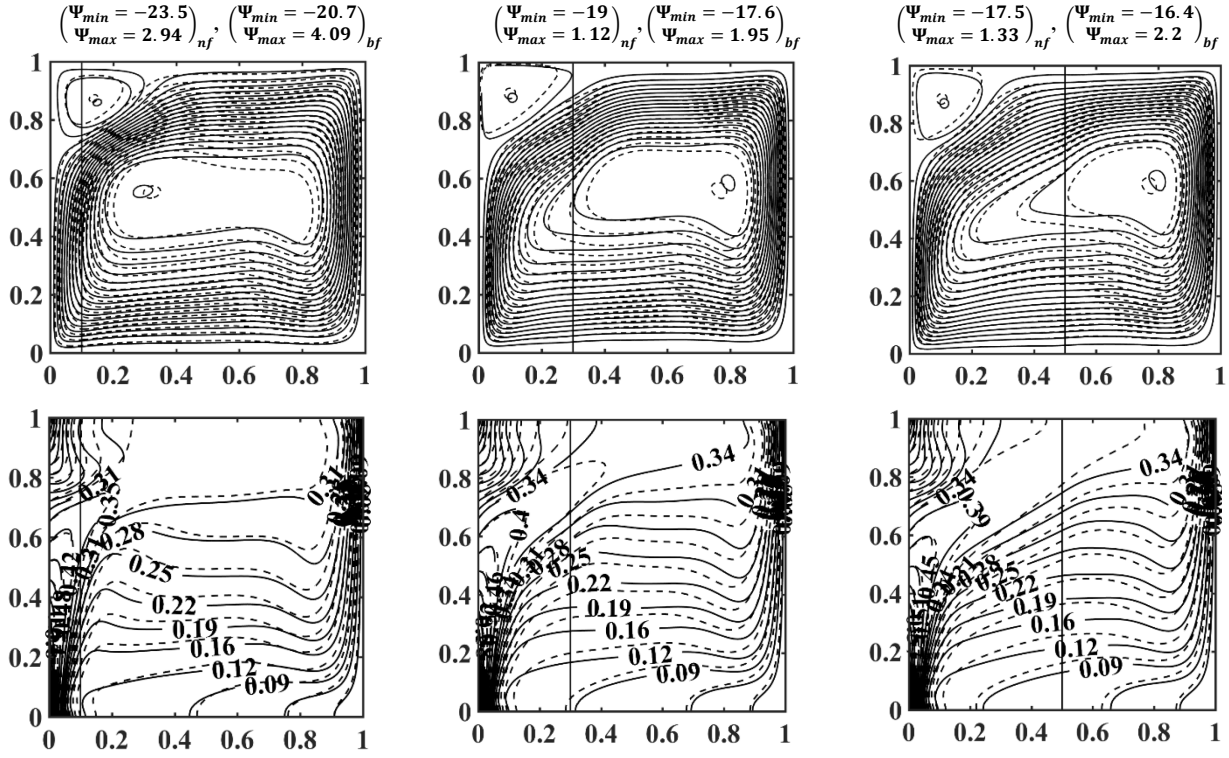

(a) $S = 0.1$ (b) $S = 0.3$ (c) $S = 0.5$

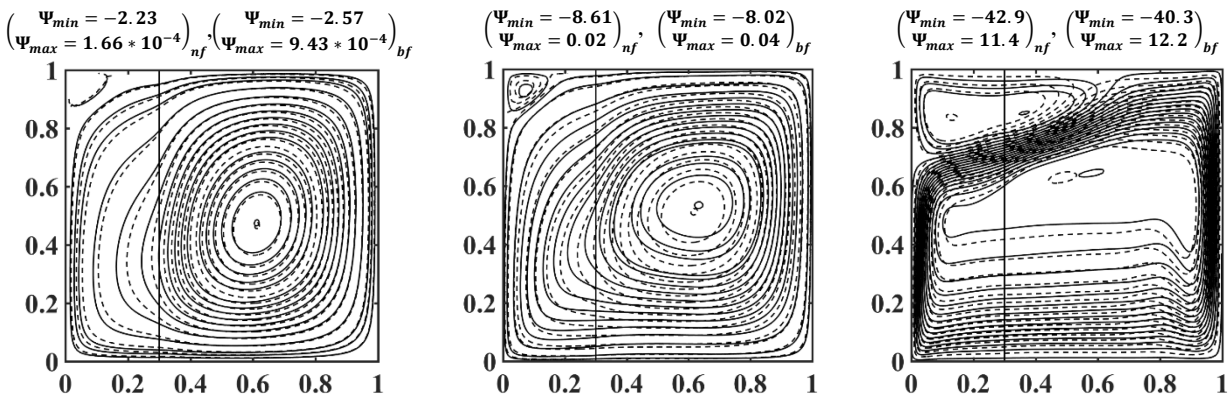

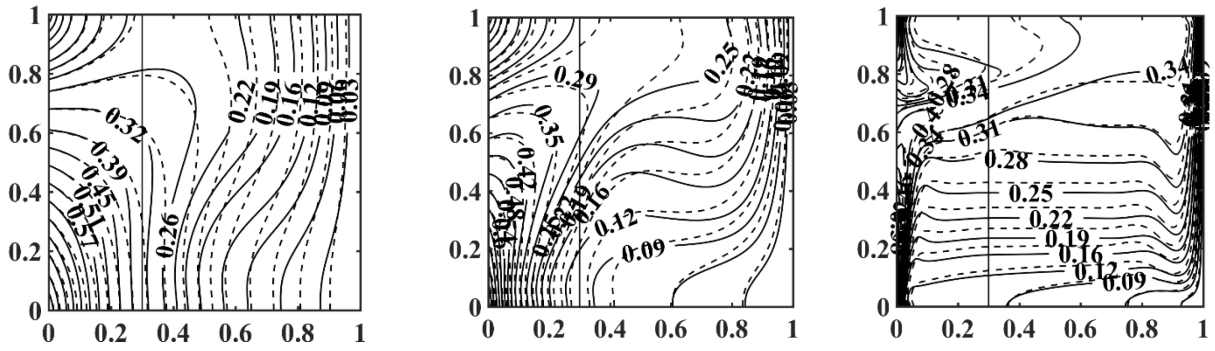

(d) $Ra = 10^4$ (e) $Ra = 10^5$ (f) $Ra = 10^7$

Figure 6: Streamlines (upper row) and isotherms (lower row) for case 1 with $\phi = 0$ (sold lines) and $\phi = 0.1$ (dashed lines) at different dimensionless parameters, (a-c) S effect when $Ra = 10^6$, $Da = 10^{-3}$ and $K_r = 1$, (d-f) Ra effect when $Da = 10^{-3}$, $S = 0.3$ and $K_r = 1$.

contours when $\theta \geq 0.31$ in the upper part of the cavity decreases with increasing porous layer thickness. Therefore, this gives an indication that increasing porous layer thickness leads to a decrease in the rate of heat transfer. The effects of the accelerated flow parameter Ra on the streamline and isotherm contour maps for $Da = 10^{-3}$, $S = 0.3$ and $K_r = 1$ are shown in Figure 6(d-f). The streamlines appear denser at high values of Ra due to the high stream function intensity of the main cell. At $Ra = 10^4$, as shown in Figure 5d, the circulation map indicates the porous layer has some effect on the transport flow from nanofluid layer to the porous layer with low flow penetration. The intensity of the secondary circulation is very low compared to the primary circulation, which filled most of the cavity area with vertical elongation parallel to the interface. It is interesting to note that adding 10% from the nanoparticles to the water leads to a reduction in the circulation strength due to increased viscous forces opposing the inertial force at any specified value of Ra. In contrast at higher Rayleigh numbers, as shown in Figures 5e and f, the intensity of the secondary cell increases, showing greater elongation, pushing the primary cell towards the lower part of the cavity to a noticeable extent, and with high penetration of the porous layer. The higher values of Rayleigh number strengthen the natural convection due to an increase in buoyancy inside the cavity, which leads to a reduction of the temperature of the heat source. Isothermally, the increase in convective heat transfer is noticeable with increasing Rayleigh number, especially for the nanofluid layer with denser

isotherms. In addition, a high spot at $\theta \geq 0.31$ occurs in the upper part of the cavity. This indicates that the diffusion of heat from the left heated source increases due to the strong circulation strength within the main cell.

Figures 7(a-c) depict the variation of the streamlines and isotherms with dimensionless permeability (Darcy number) for $Ra = 10^6$, $S = 0.3$, and $K_r = 1$. These figures show that the susceptibility of the porous layer to penetration by the nanofluid depends on the Darcy number value. At $Da = 10^{-5}$, as shown in Figure 7a, the main cell is confined to the region around the nanofluid layer, with lower penetration of the porous layer. Figure 7b and c shows that increasing Da to 10^{-2} and 10^{-1}, respectively, results in an increase in the intensity of the main cell accompanied by the appearance of a weak secondary cell at the upper left corner of the cavity. The main cell centre at high values of Da moves from the nanofluid layer towards the porous layer close to the left heated wall, whilst conversely remaining in the region of the nanofluid layer for $Da = 10^{-3}$, as shown in Figure 6b. It is interesting to note that the streamlines with low Darcy number are more effective with the addition of 10% of nanoparticles to the pure fluid than the higher values. This can be illustrated by the $|\Psi_{min}|$ values, where for $Da =$

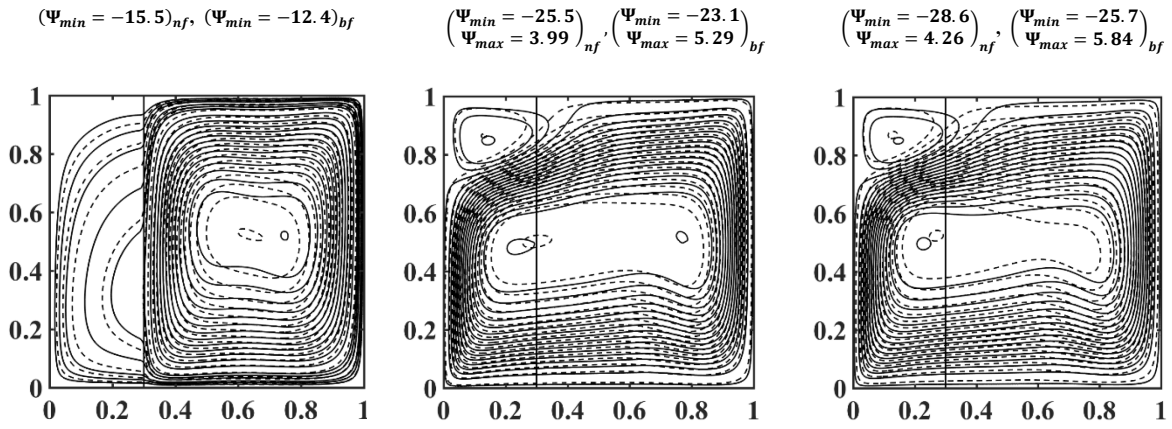

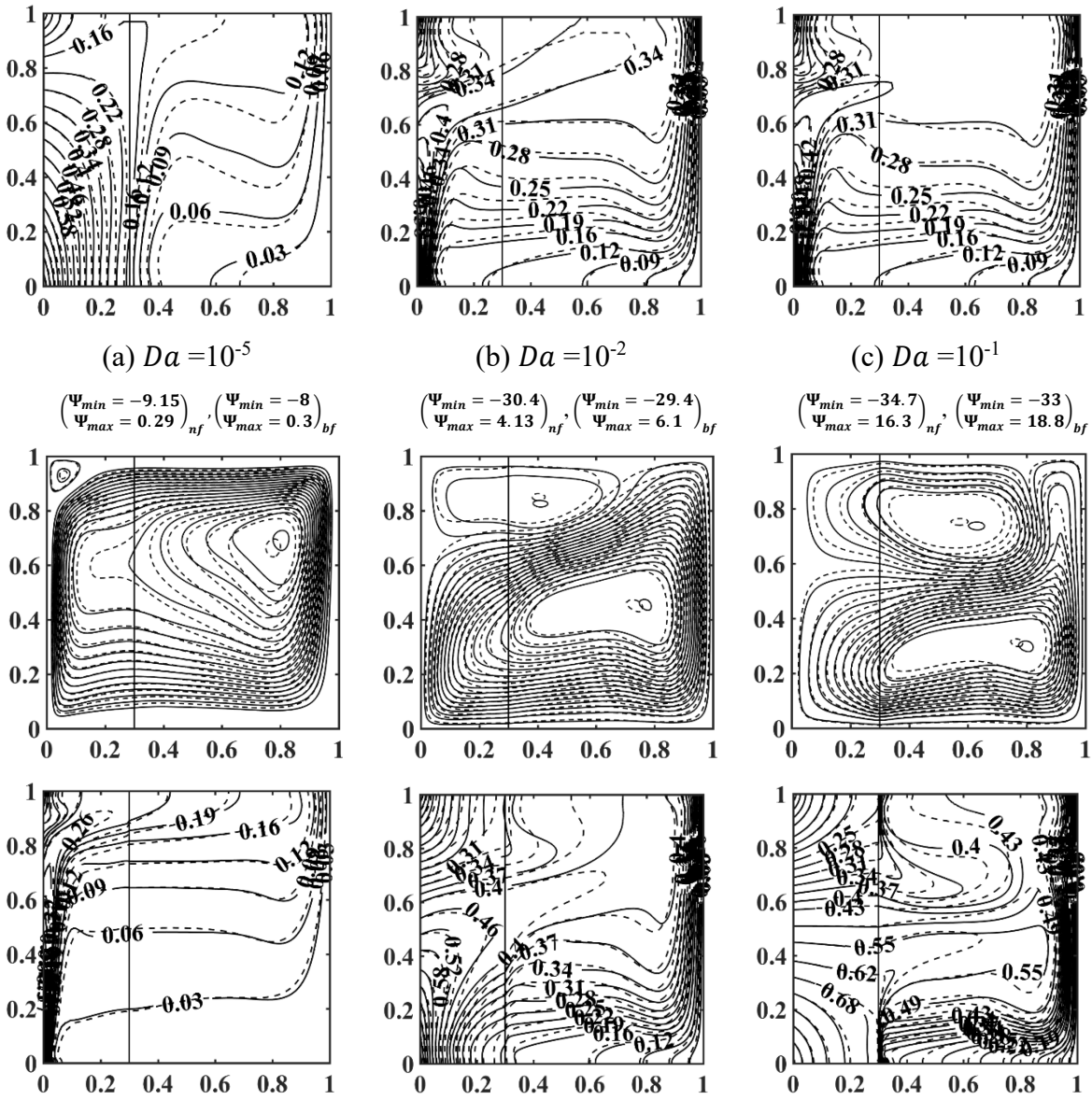

Figure 7: Streamlines (upper row) and isotherms (lower row) for case 1 with ϕ = 0 (sold lines) and ϕ = 0.1 (dashed lines) at different dimensionless parameters, (a-c) Da effect when $Ra = 10^6$, S = 0.3 and K_r = 1, and (d-f) K_r effect when $Ra = 10^6$, $Da = 10^{-3}$and S = 0.3.

10^{-5}, 10^{-2} and 10^{-1}, the percentage variations in $|\Psi_{min}|$ are 25%, 10.4% and 11%, respectively. The isotherm figures show how the Darcy number can be used as a controlling parameter to translate the convection from the nanofluid layer to the porous layer. The high density of the isotherm lines appearing close to the vertical walls due to the increasing in magnitude of Da is indicative of the convective heat transfer within the enclosure. This causes the temperature of

the heat source to be reduced with an increasing permeability of the porous layer matrix. The effect of thermal conductivity ratio, K_r, on the streamlines and isotherms counters for Ra = 10^6, Da = 10^{-3} and S = 0.3 is illustrated in Figure 7(d-f). Streamlines appear with two different cells when K_r = 0.1, as shown in Figure 7d. The centre of the clockwise primary cell is located adjacent to the right cold wall with steeper streamlines on the left-hand heated and right-hand cooled walls while the weak, anticlockwise-circulating secondary cell is located at the upper left corner of the cavity. At K_r = 5 (see Figure 7e), the stream function of the main clockwise and the upper left counter-clockwise cells is higher values than that at K_r = 0.1 and also compressing the primary cell by the secondary cell towards the lower right corner of the cavity. The centre of the primary and secondary cells moves away from the left-hand heated source wall towards the right-hand cold wall results in reduced penetration of the nanofluid flow into the porous layer. This pattern increases up to K_r =100, with a lower density in the streamlines in the region of the left-hand heated wall. This augmentation in the circulation strength is attributed to an increased thermal conductivity ratio (porous/nanofluid). At higher K_r, the increasing strength and cell size of the upper, anticlockwise-circulating secondary cell causes the hot nanofluid to return the heat towards the upper part of the heat source, which leads to a decrease in heat transfer. However, at lower values of K_r, the convection heat transfer is dominant within the cavity. Isothermally, the convection is transmitted from the nanofluid layer to the porous layer at the lower thermal conductivity ratio of K_r=0.1, whilst when the isotherm lines crosses the left-hand heated wall at higher values of K_r, signifying conductive heat transfer

4.1.2 *Horizontal porous-nanofluid layers (case 2)*

Figure 8 illustrates the contours of streamlines (upper row) and isotherms (lower row) for different effective dimensionless parameters when the nanofluid layer is overlying the

porous layer. Figure 8(a-c) shows the variation of flow and isotherm patterns inside the enclosure with varying porous layer thickness, S, as $Ra = 10^6$, $Da = 10^{-3}$, and $K_r = 1$. As in the previous case, due to the linear thermal boundary conditions applied to the left-hand sidewall of the cavity, the nanofluid inside both layers rises along the left-hand heated wall and flows down along the cooled right-hand wall, causing two circulating regions. The primary circulation covered most of the cavity, rotating in a clockwise direction, while the secondary circulation ran in an anticlockwise direction and appeared in the upper region of the left-hand heated wall. Figure 8a illustrates the low penetration of the streamlines into the porous layer as compared with case 1, which gives an indication of effect of the porous-nanofluid layers' orientation. It is interesting to note that the centre of the main cell remains close to the left-hand heated wall while the secondary cell tends to compress the main cell towards the porous layer, which is in contrast with case 1 where the upper circulation tends to push the main cell towards the right-hand cooled wall. $|\Psi_{min}|$ shows that the intensity of circulations, in this case, is stronger than for case 1 for different thicknesses of the porous layer. However, the addition 10% of nanoparticles to the pure fluid leads to a lower increase in the percentage of $|\Psi_{min}|$ values compared to case 1 except at S = 0.3, where for S = 0.1, 0.3 and 0.5, the gain in percentages of $|\Psi_{min}|$ are 10.8%, 8.3% and 5.5%, respectively. Although the increases in percentage are lower in this case, it is expected that the intensity of circulation might actually increase convective heat transfer. The isotherms in the vicinity of the heat source, in this case, are denser than in case 1. The temperature contour with $\theta \geq 0.31$ is also pushed towards the top left corner of the cavity with a relatively lower thickness of the thermal boundary (steeper lines) compared to case 1, and this thickness increases with increasing thickness of the porous layer, especially for the nanofluid contour. Figure 8(d-f) shows the effect of Rayleigh number on the streamline and isotherm contour maps for case 2 with $Da = 10^{-3}$, S = 0.3 and $K_r = 1$. The contour map for the streamlines in the upper panel of Figure 8d depicts the flow inside the

cavity at $Ra = 10^4$. It is clear that the porous layer has an effect on the transport flow within the porous layer, with low penetration of the nanofluid. The intensity of the secondary cell is very low as compared with the main cell strength. The intensity of the main circulation is also low, with horizontal elongation in a semi-circular shape parallel to the interface between the porous and nanofluid layers when compared with case 1. A significant change in the flow pattern inside the cavity occurs with increasing Rayleigh number when $Ra = 10^5$ up to $Ra = 10^7$, as shown in Figure 8e and f, respectively. The secondary cell at the upper left corner appears with high intensity above the primary cell, which has relatively more intensity than in case 1 (see Figure 6f). The secondary cell tends to compress the main cell, leading to the generation of two poles whose

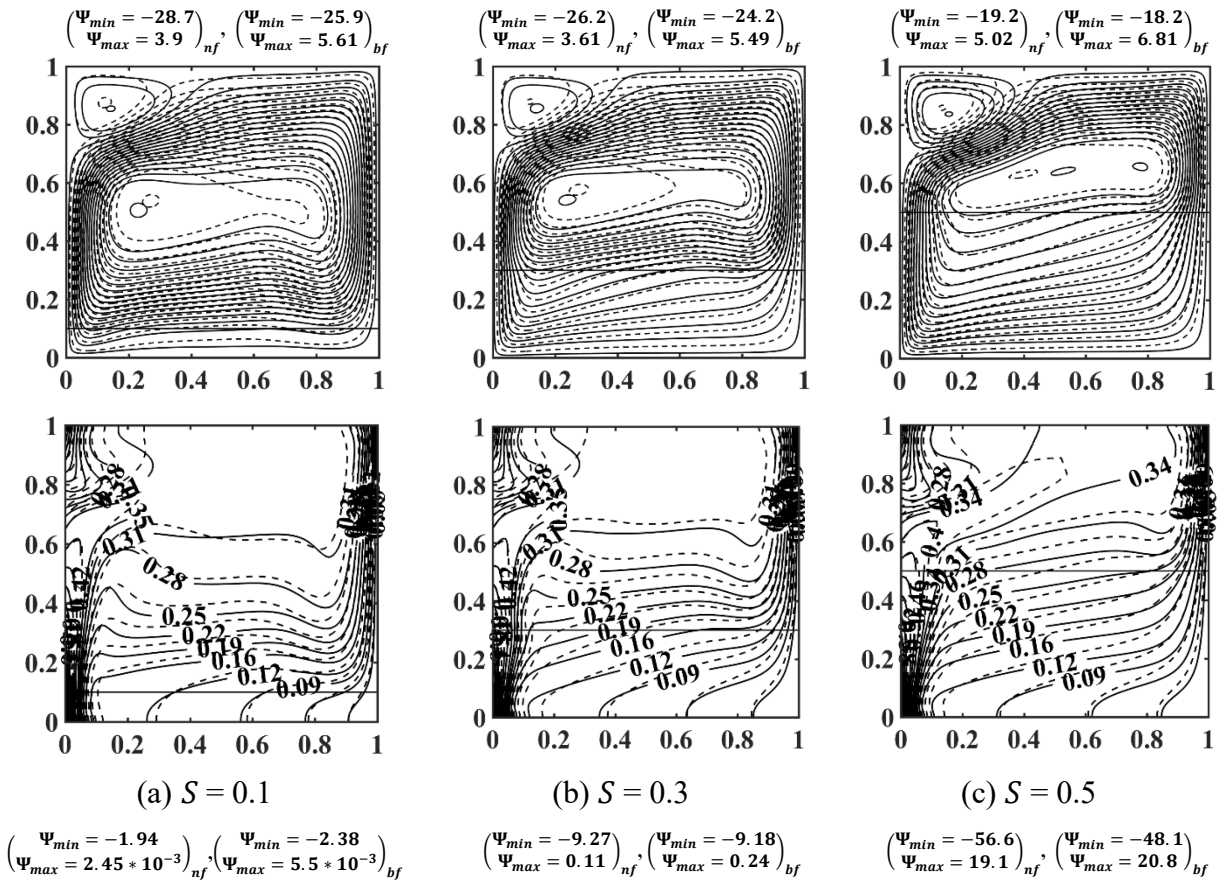

(a) $S = 0.1$ (b) $S = 0.3$ (c) $S = 0.5$

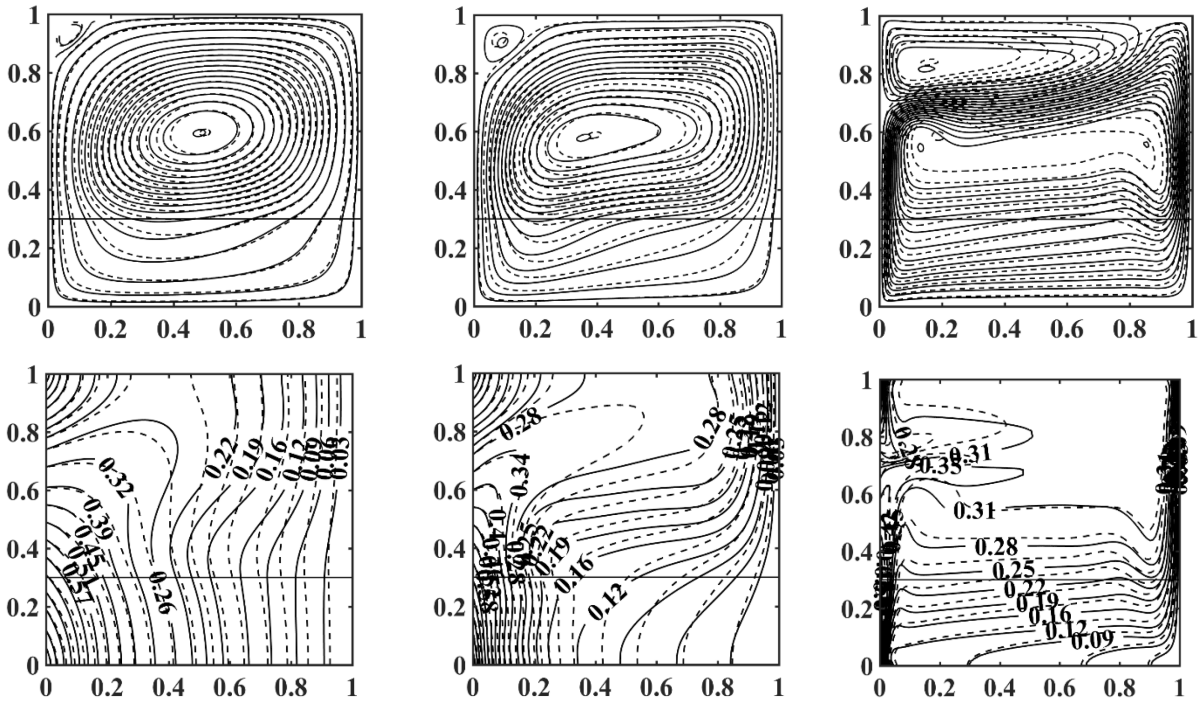

(d) Ra=10^4 (e) Ra=10^5 (f) Ra=10^7

Figure 8: Streamlines (upper row) and isotherms (lower row) for case 2 with ϕ = 0 (sold lines) and ϕ = 0.1 (dashed lines) at different dimensionless parameters, (a-c) S effect when Ra = 10^6, Da = $10^{-3}$and K_r = 1, (d-f) Ra effect when Da = 10^{-3}, S = 0.3 and K_r = 1.

centres are close to the cooled right-hand and hot left-hand walls. Isothermally, the thickness of the thermal boundary layer is less in case 2 as compared with case 1 due to the augmentation of circulation intensity when the circulation centre is closer to the left and right vertical walls.

Figure 9(a-c) illustrates streamline (upper row) and isotherm (lower row) contours as Ra = 10^6, S = 0.3 and K_r = 1 for different values of Da. It can be observed from the streamline contour map that the nanofluid flow circulation is strongly dependent on the Darcy number. At Da = 10^{-5}, as shown in Figure 9a, two cells are observed in the cavity. One is the strong main cell with a clockwise flow circulation, and which is dominant across the majority of the cavity, while the weak anticlockwise flow circulation appears at the upper left corner of the cavity with low penetration into the porous layer. It is interesting to note that the streamlines at Da =10^{-5} for this case have a higher value of $|\Psi_{min}|$ = 20.5 for nanofluid and $|\Psi_{min}|$ = 18.7 for the

pure fluid, where the streamlines behave in a different manner than in case 1, as seen in Figure 7a. As Da increases, the penetration of the nanofluid flow increases with higher circulation intensities. The addition of 10% Cu nanoparticles by volume to the pure fluid result in percentage gains in $|\Psi_{min}|$ for Da = 10^{-5}, 10^{-2} and 10^{-1} of 9.6%, 11.37% and 11.53%, respectively. Although the percentage gain for this case at Da = 10^{-5} is lower than in case 1, it seems that a higher density in the temperature gradient forms within the thermal boundary layer in the nanofluid layer along the left and right walls as compared to the vertical walls in case 1. Another comparison between these cases is that the isotherm $\theta \geq 0.31$ for Da = 10^{-2} and 10^{-1} has more spots in the upper part of the cavity compared to case 1 with greater diffusion of the heat from the heat source, signifying that the enhancement of the convective heat transfer for case 2 is greater than for case 1.

Figure 9(d-f) displays the streamlines (upper row) and isotherms (lower row) with Ra = 10^6, Da = 10^{-3} and S = 0.3 for different thermal conductivity ratios (K_r). Common streamline patterns of the flow within the cavity show a similar trend to the primary and secondary cells inside the cavity. The location of the main cell core centre is close to the left-hand heated sidewall while the secondary circulation is confined to the upper left corner of the cavity. The intensity of the primary and secondary circulations increases with increasing thermal conductivity ratio. At K_r = 0.1, the primary cell covered most of the cavity area with low penetration of the porous layer, as shown in Figure 9d. It is interesting to note that the stream function strength of the primary cell is significantly greater than for case 1 at lower values of K_r. In addition, the core centre of the primary cell moves towards the left-hand heated wall causes denser streamlines along the vertical walls in the nanofluid layer. Figure 9e shows the

$\begin{pmatrix}\Psi_{min}=-20.5\\ \Psi_{max}=1.13\end{pmatrix}_{nf}, \begin{pmatrix}\Psi_{min}=-18.7\\ \Psi_{max}=2.02\end{pmatrix}_{bf}$ $\begin{pmatrix}\Psi_{min}=-28.4\\ \Psi_{max}=4.31\end{pmatrix}_{nf}, \begin{pmatrix}\Psi_{min}=-25.5\\ \Psi_{max}=5.94\end{pmatrix}_{bf}$ $\begin{pmatrix}\Psi_{min}=-29\\ \Psi_{max}=4.23\end{pmatrix}_{nf}, \begin{pmatrix}\Psi_{min}=-26\\ \Psi_{max}=5.88\end{pmatrix}_{bf}$

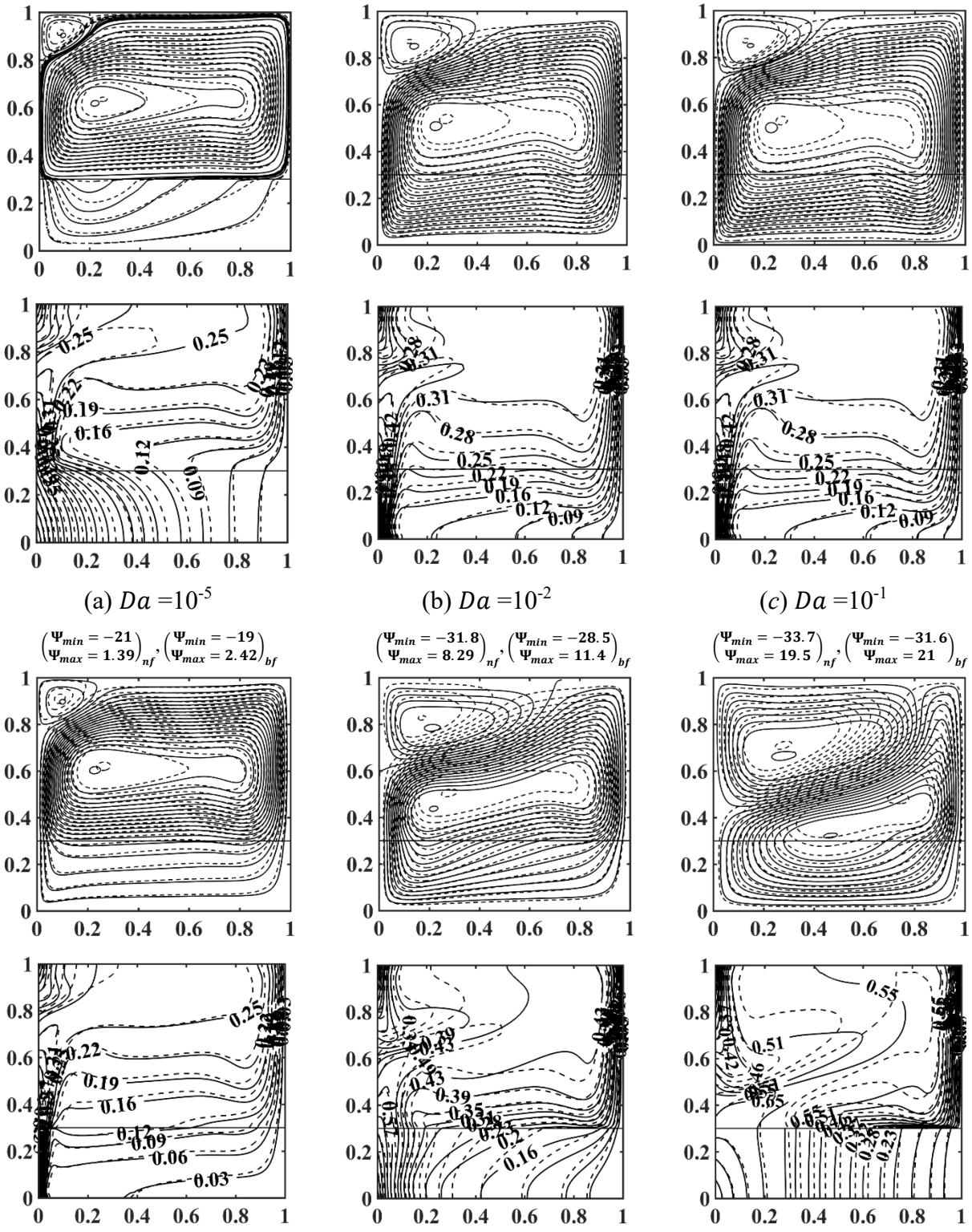

Figure 9: Streamlines (upper row) and isotherms (lower row) for case 2 with ϕ = 0 (sold lines) and ϕ = 0.1 (dashed lines) at different dimensionless parameters, (a-c) Da effect when Ra = 10^6, S = 0.3 and Kr = 1,and (d-f) K_r effect when Ra = 10^6, Da = 10^{-3} and S = 0.3.

streamlines of the fluid flow inside the cavity for K_r = 5 have greater intensity and elongation of the secondary cell, causing the compression of the primary cell towards the porous layer.

Another significant point is that the core centres of the nanofluid cells, due to the additional 10% Cu nanoparticles present, tend to remain in the nanofluid layer compared to the pure fluid cells, which leads to the stream function of the nanofluid having greater strength than the pure fluid. As K_r increases, the pattern of the fluid flow within the cavity continues up to K_r = 100 though with greater elongation of the secondary cell, which causes the rotation of the flow towards the left-hand heated wall. Isothermally, the horizontal isotherm lines indicate convective heat transfer, while the vertical isotherm lines indicate conductive heat transfer. The isotherm lines are denser and closer to the left and right vertical walls due to the elongation of the cells towards the vertical walls with the reduced thickness of the thermal boundary layer along the vertical walls. At K_r = 0.1 with the isotherm $\theta \geq 0.25$, the convective heat transfer is dominant in the cavity, even at the porous layer, and the heat transport at the top portion of the cavity is more diffused compared to case 1. As K_r increases towards 100, the convective heat transfer remains confined to the nanofluid layer, while the conductive heat transfer appears in the porous layer when the thermal boundary layer is relatively thick. The high density of the isotherms close to the left and right walls in the nanofluid layer resulted in significant temperature diffusion from the heat source when compared to case 1. However, negative heat transfer occurs due to the secondary cell effects that lead to the transmission of the heat energy from the nanofluid towards the heat source. As expected, the heat transfer decreases with increasing K_r, especially in case 1.

4.2 Velocity components (U, V and R)

The distributions of the velocity components U, V and R, are examined at the interface between the porous-nanofluid layers along the Y-axis and X-axis for case 1 and case 2, respectively, at S = 0.3, ϕ = 0.1 and K_r = 1 with Ra = 10^4 and 10^6 for different Da values, as shown in Figure 10.

4.2.1 *Vertical porous-nanofluid layers (Case 1)*

Figure 10a shows the variation of velocity profile components for different Da values at the interface between the porous-nanofluid layers for case 1 as S = 0.3, ϕ = 0.1 and K_r = 1 when Ra = 10^4 and 10^6. Increasing the Rayleigh number causes a significant augmentation in the velocity components within the cavity due to the strong effect of the buoyancy force. The

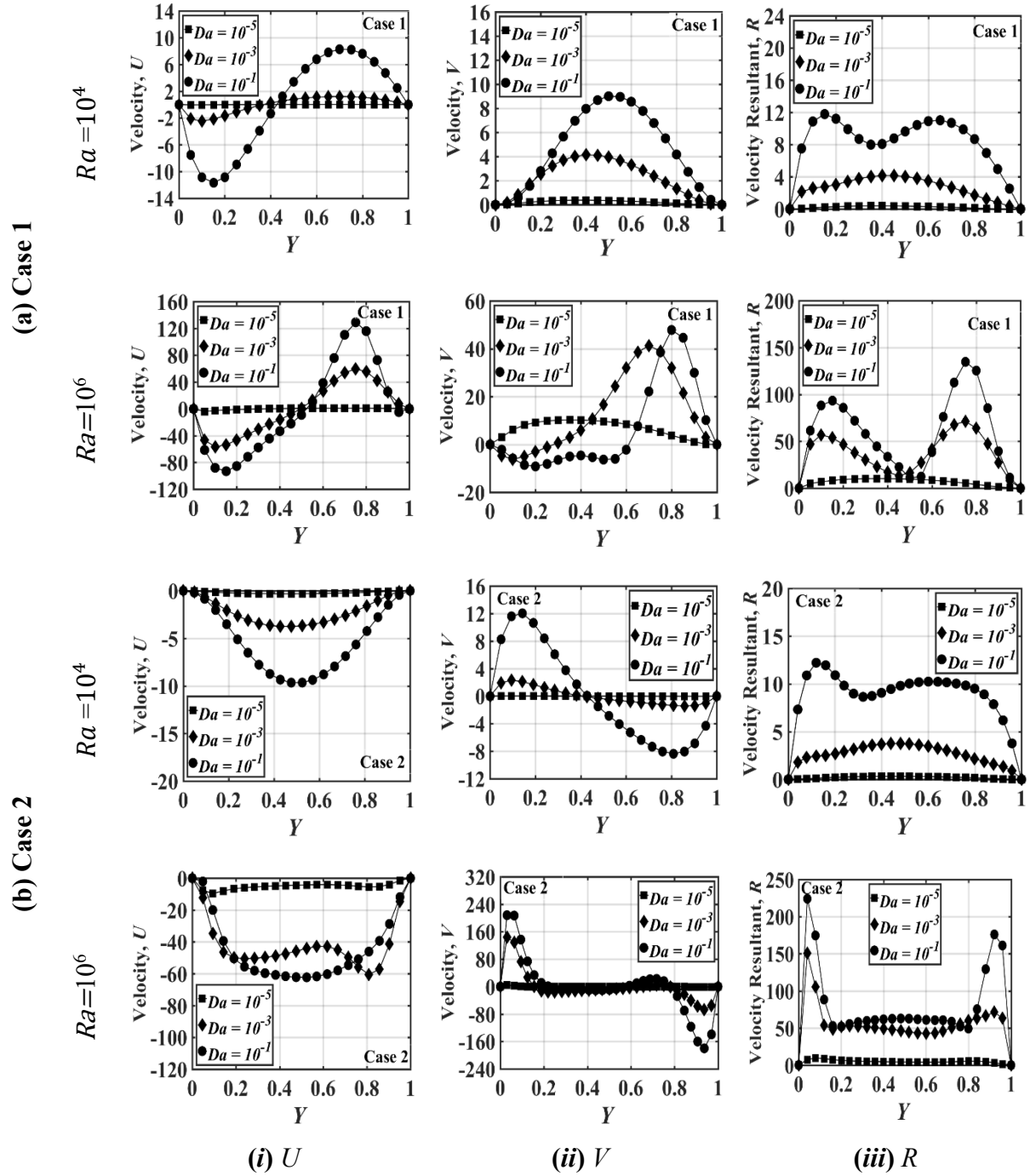

Figure 10: Variation of velocity profile components **(*i*)** U, **(*ii*)** V, and **(*iii*)** R at the interface line of **(a)** case 1 and **(b)** case 2 for different Darcy numbers as S =0.3 , ϕ = 0.1 and K_r =1 at Ra = 10^4 and Ra =10^6.

flow strength of the nanofluid increases and the maximum and minimum velocity components at the interface of the enclosure with Da =10^{-1} become greater than those for Da = 10^{-5}. This is attributed to the increased permeability of the porous layer causing a reduction in the resistance offered by the porous layer on nanofluid flow, resulting in an increase in velocity. Figure 10a*i* depicts the effects of the Darcy and Rayleigh numbers on the horizontal velocity component at the interface for case 1. It is interesting to note that for the velocity profile at Ra = 10^4, it appears that the velocity of the nanofluid flow towards the upper part of the interface is lower than the flow at the bottom of the interface. This is because of the hydrodynamic resistance offered by the porous layer. However, this pattern takes the opposite trend with increasing Ra values because of the density of the streamlines at approximately Y = 0.7. The negative value of the horizontal velocity close to the upper adiabatic wall attributes to the anticlockwise motion of the secondary cell. Figure 10a*ii* shows the effect of the permeability of the porous layer on the vertical velocity component along the interface for case 1 with different values of Ra. Monotonic parabolic curves are observed at Ra = 10^4. Increasing Ra to 10^6 causes a disturbance in this behaviour due to the non-uniform pattern of the streamlines at the interface with higher values of Ra at approximately Y = 0.7 and 0.8 for Da = 10^{-3} and 10^{-1}, respectively. This attributes to the high buoyancy force that introduced due to increasing the Rayleigh number and high penetrating through the porous layer due to increasing the Darcy number. This leads to that, the main cell moves strongly towards the porous layer. The local distribution of the resultant velocity component for case 1, as shown in Figure 10a*iii*, clarifies the effect of the Darcy number on the nanofluid flow inside the cavity. The velocity resultant at Da =10^{-5} is almost zero compared to the higher value of Da, which means less hydrodynamic resistance with high permeability of the porous matrix. At Ra = 10^4 with Da = 10^{-1}, the resultant

of the velocity component reaches a maximum at about Y = 0.1 and 0.7 while its minimum occurs at about Y = 0.4. Increasing Ra causes the minimum values to approach zero between Y = 0.4 and 0.6 due to the localization of the cell core at this height inside the cavity.

4.2.2 *Horizontal porous-nanofluid layers (Case 2)*

Figure 10b shows the effect of the permeability parameter (Da) on the velocity components U, V and R for case 2 as S = 0.3, ϕ = 0.1 and K_r= 1 when Ra = 10^4 and 10^6. At Ra = 10^4, as shown in Fig 10b*i*, the monotonic curves with negative horizontal velocity values appear at the interface between the porous-nanofluid layers. The symmetric behaviour with negative values results from the main circulation streamlines being undisturbed where the flow turns towards the left wall, with a maximum value at X = 0.5. Increasing the Rayleigh number to 10^6 leads to an increase in velocity along the interface with considerable disturbance due to the non-uniform paths of the main vortex streamlines in this region.

Figure 10b*ii* shows the variation of the vertical velocity profile for case 2 for different *Da* values along the horizontal interface line at Y = 0.3 for ϕ = 0.1 and K_r = 1 when Ra = 10^4 and 10^6. The effect of changing the Darcy number values seems clearer at lower values of Ra. Increasing Da causes the vertical velocity component to increase near the vertical walls where the velocity near the left wall is relatively greater than near the right wall. This is due to the increase of the buoyancy force close to the heated wall. The increase in *Ra* value causes a change in the trend of the vertical velocity profile at the interface from an oscillatory to a uniform pattern with zero values between X = 0.2-0.6, with large velocities near the vertical walls. This is because of the elongation of the main cell along the interface line. Figure 10b*iii* illustrates the velocity resultant of the nanofluid flow for different *Da* values along the horizontal interface for case 2 as ϕ = 0.1 and K_r = 1 when Ra = 10^4 and 10^6. It seems that the pattern seen for the velocity resultant in this case is similar to the previous case, though with a

relatively greater strength than for case 1. However, this pattern breaks with increasing Ra, with a uniform velocity distribution between X = 0.2 - 0.8 with large velocities near the vertical walls of the cavity. This is due to dominant and elongated main circulation pattern along the interface. In general, the resultant velocity for case 2 is greater than for case 1. This may be because of the effect of the direction of the porous-nanofluid layers. Therefore, it is expected that the heat removal from the left-hand heated wall for case 2 will be greater than for case 1.

4.3 Dimensionless temperature distribution, θ

In this section, the dimensionless temperature distribution θ along the interface at X = 0.3 for (i) case 1 and Y = 0.3 for (ii) case 2 will be examined in terms of various effective dimensionless parameters such as (a) Ra effect, (b) K_r effect, and (c) S effect, as shown in Figure 11.

4.3.1 *Vertical porous-nanofluid layers (Case 1)*

Figure 11i (a-c) illustrates the dimensionless temperature distribution versus distance along the vertical interface for case 1 at X = 0.3. In Figure 11ia, the temperature distribution shows a higher value at the lower value of Ra when Y = 0 due to conductive heat transfer and a minimum value at the upper part of the interface while this pattern is reversed for high values of Ra due to the increase in buoyancy, which in turn dominants the convective heat transfer. The effect of increasing the thermal conductivity ratio (porous to nanofluid) on the temperature distribution along the interface for case 1 is illustrated in Figure 11ib. At Y = 0, the temperature increases with increasing K_r due to the density of the isotherms at the bottom of the vertical interface line. The temperature increases monotonically along the interface for low values of K_r up to Y = 1, while this behaviour is reversed for high values of K_r. This gives an indication that the temperature of the heat source for the heated wall is decreased with a reducing thermal conductivity ratio. The effect of increasing the porous layer thickness on the temperature

profile along the interfaces line for case 1 is illustrated in Figure 11*i*c. The temperature decreases with increasing S at Y = 0 - 0.8 because of the walls' distances from the thermal source. However, at $Y \geq 0.8$, the temperature profile behaves in the opposite manner due to the vertical interface being further away from the left-hand heated wall, where there is a high temperature at the upper part of the enclosure. Increasing the porous layer thickness S means increasing the flow resistance, which results in a reduced heat removal from the left-hand heated wall.

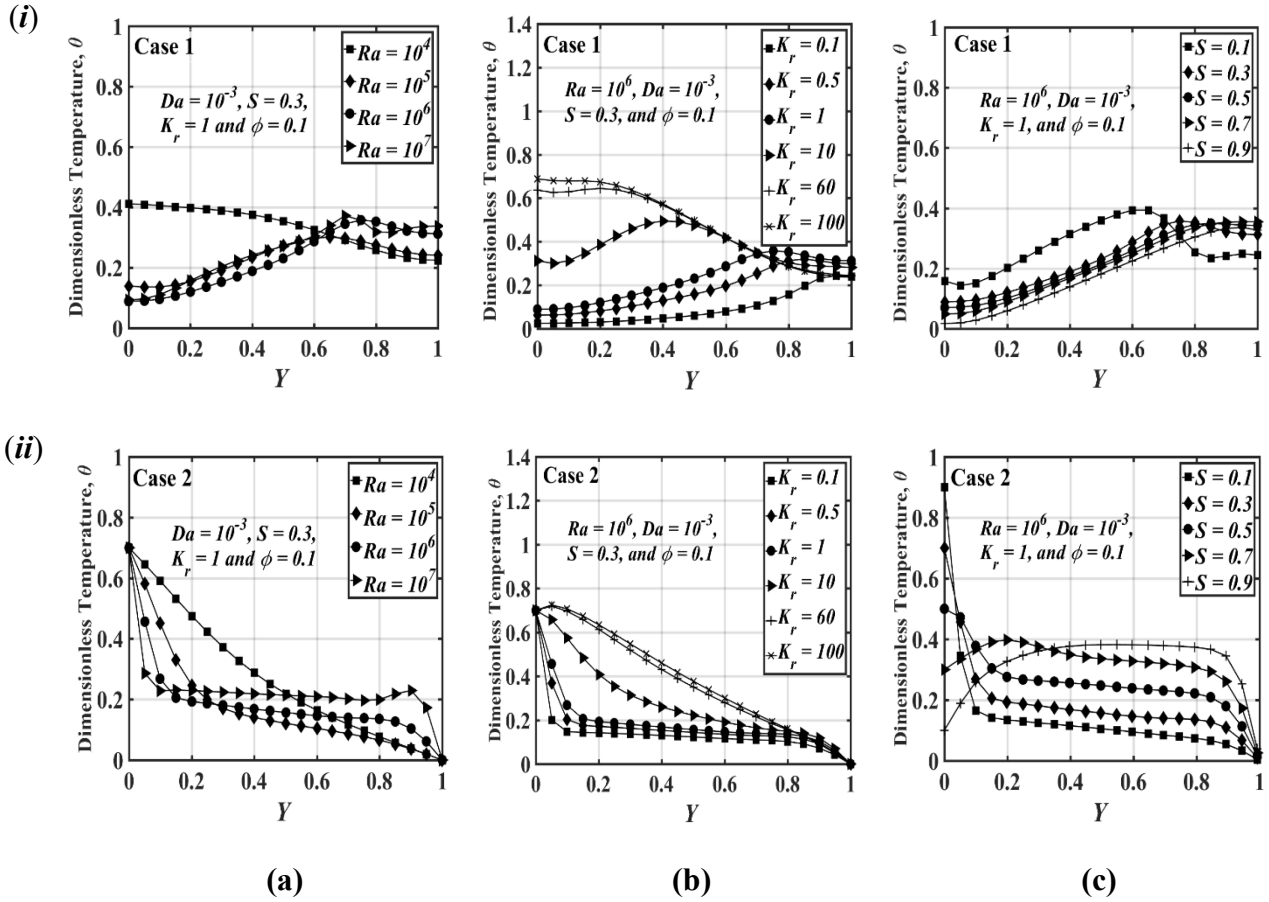

Figure 11: Local distribution of dimensionless temperature along the interface line for ***(i)*** case 1 and ***(ii)*** case 2 with different dimensionless parameters **(a)** Ra effect, **(b)** K_r effect, and **(c)** S effect.

4.3.2 *Horizontal porous-nanofluid layers (Case 2)*

Figure 11*ii* (a-c) illustrates the dimensionless temperature distribution versus distance along the interface for case 2 at Y = 0.3 for various parameter effects. At X = 0, θ = 0.7 for all values of Ra because the base of the horizontal interface is located on the left-hand heated wall at Y = 0.3, as shown in Figure 10*ii*a. At $X \leq 0.3$, the temperature distribution sharply decreases with increasing Ra, with a minimum value at $Ra = 10^7$, while the opposite can be seen for $X > 0.3$. This indicates that the removal of heat from the heat source increases with increasing Rayleigh number. The variation in the temperature profile along the interface with different values of thermal conductivity ratio for case 2 is illustrated in Figure 11*ii*b. The temperature profile sharply decreases at $X < 0.2$ with decreasing K_r values. Low K_r values result in a decrease in the temperature distribution along the interface due to the dominance of the main circulation along the interface with the convective heat transfer mode at the porous layer. At high values of K_r, a linear temperature distribution appears along the interface. Figure 11*ii*c shows the effect of changing S values on the temperature distribution along the interface between the nanofluid and the porous layers. It is interesting to observe that the temperature distribution for case 2 is greater than for case 1 at X = 0 for all values of S due to the linear heating. Increasing S leads to a rise in the temperature inside the enclosure due to an increase in the effects of the area resistance on the nanofluid flow offered by the porous layer, which leads to a decrease in the stream function strength of the main cell. This also causes an increase in the thermal boundary layer thickness as shown in Figure 8(a-c). At a constant value of S, the temperature distribution decreases along the interface due to the distance from the left-hand heated wall. It is clear that in case 2, the temperature along the interface will be a maximum at X = 0 when S = 0.1, while the opposite behaviour is seen along the interface up to X = 1. Conversely, this pattern satisfies only at the upper part of the interface in case 1 where the temperature increases with decreasing porous layer thickness along the interface up to Y = 0.7.

This change in the temperature distribution pattern can be attributed to the effect of the porous-nanofluid layers' orientation, which causes results in different behaviour of the streamlines in the cavity.

4.4 Heat transfer rate: Local Nusselt number

The distribution of the local Nusselt number is illustrated in Figure 12 under the different effects of selected parameters such as Darcy number (a) and thermal conductivity ratio (b). The left columnn represents the local Nusselt number on the left-hand heated wall (Nu_l) while the right columnn represents the local Nusselt number on the right-hand cooled wall (Nu_r). The upper and lower panels represent case 1 and case 2, respectively.

The upper panel plots of Figure 12a show the local Nusselt number as a function of distance along the left and right walls for case 1 when $Ra = 10^6$, $\phi = 0.1$, $K_r = 1$ and $S = 0.3$ for different values of Da. The maximum value of the local Nusselt number Nu_l on the left heated wall (left column) is located at the bottom portion of the left heated wall that is having a maximum temperature of the enclosure due to the linearly heated left sidewall. At $Y = 0$, the positive value of the local Nusselt number (heat transport from the wall towards the nanofluid) increases with increasing Da due to an increase in the porous layer's permeability with high streamline strength due to the convective heat transfer mode within the cavity. At $Y \geq 0.4$, Nu_l is negative (heat is transported from the nanofluid towards the wall) signifying the reverse heat transfer with a minimum Nu_l at the top portion of the hot left-hand sidewall of thy enclosure. The minimum change in Nu_l is obtained with low Darcy number ($Da = 10^{-5}$) due to the high resistance offered by the porous matrix. A comparison of effects of changing Da values on the local Nusselt number under the same conditions between case 1 and case 2 can be seen in the left-hand column and lower panel plot in Figure 12a, which represents case 2; and it seems a similar trend in Nu_l is observed for case 1. However, the maximum value of Nu_l for $Da = 10^{-}$

^{2} when Y = 0 in case 2 is greater than the equivalent value for case 1 under the same conditions. This attributes to that, the stream function value in case 2 is higher strength than case 1. Another significant point that can be determined from this figure is that some retarding of Nu_l values along the vertical left sidewall at Da = 10^{-5} which is observed that more receiving heat from the heat source in case 2 compared to case 1. Increasing Da from Da = 10^{-5}-10^{-1}causes the right-hand cold sidewall to receive more heat from the nanofluid, which leads to the local Nusselt number taking a negative value. The maximum heat that received by the right-handside wall is focused at Y = 0 in the case1 while it is maximum values at Y = 1 in case 2. This difference is due to the main cell effects on the guidance of the hot nanofluid along the right-handside wall. At Da = 10^{-5}, Nu_r appears as a different behaviour as shown in the right column of Figure 12a. In case 2, Nu_r is almost constant values up to Y = 0.3 due to the dominance of the conductive heat transfer mode at the porous layer. Nu_r values smoothly increase when Y $>$ 0.3 with maximum values at the top portion of the right-hand cold wall due to the high convective heat transfer inside the enclosure.

(a)

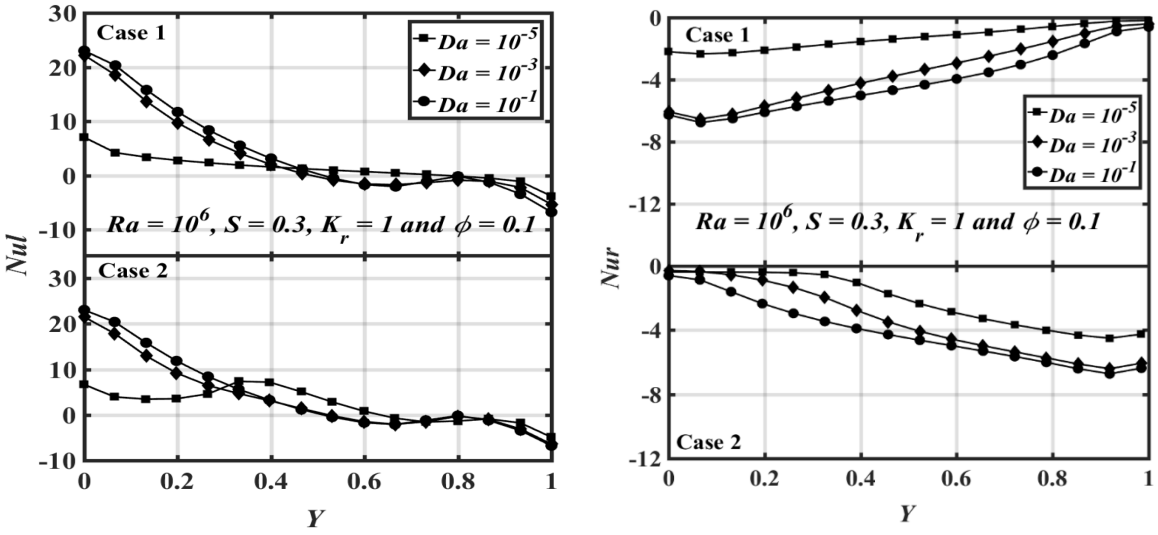

(b)

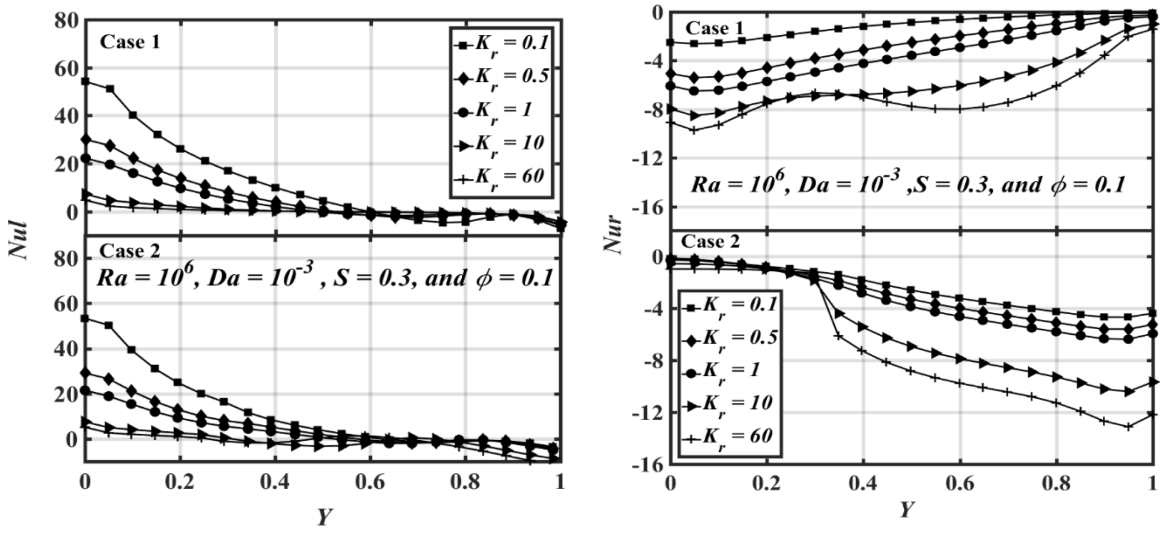

Figure 12: Variation of the local Nusselt number along the left hot wall (left column) and the right cold wall (right column) with different dimensionless parameters **(a)** Da effect and **(b)** K_r effect.

Figure 12b shows the effect of K_r on the local Nusselt number along the left and right walls of the cavity for case 1 and 2, as shown in the left and right columns of the figure at Ra = 10^6, Da = 10^{-3}, ϕ = 0.1 and S = 0.3. The upper panel plot and left column of Figure 12b depicts the effect of K_r on Nu_l along the left-hand hot wall. The trend for Nu_l is similar in behaviour to that of the effects of Da due to the linearly heated left-hand wall. Increasing K_r value results in a decrease in the heat transfer rate that results from the dominance of the conductive heat transfer along the left-hand heated wall up to the upper part of the heated wall with a negative value of Nu_l. The negative value of Nu_l implies the reverse heat transfer that results from increasing the strength of the secondary cell. In case 2, Nu_l behaves in a similar manner to the variation for case 1 except some difference at the top portion of the left wall due to the high dense of the isotherm lines for case 2 compared to case 1. The upper panel plot of Figure 12b in the right column represents the variation of Nu_r for case 1 along the right-hand cold wall at Ra = 106, Da = 10-3, ϕ = 0.1 and S = 0.3 for different K_r. The largest negative values for Nu_r are located at the bottom section of the right wall especially at the high value of K_r.This is die to the moving of the main cell center location at the lower part of the right-

handside wall. Nu_r increases with increasing K_r, and vice-versa, as compared to Nu_l. This is because, with increasing K_r, the density of the isotherms is greater along the right-hand cold wall, especially at the top of the wall. The oscillatory behaviour of Nu_r at K_r = 100 may stem from the effect of the plume of isotherm lines towards the dense lines of the thermal boundary layer along the right-hand cold wall (see Figure 7f). In case 2 (lower panel of the right column of Figure 12b), under the same conditions and compared with case 1, the maximun values of Nu_r appear at the top portion of the right-handside wall which is relatively constant values when Y $<$ 0.3 for different K_r values. This is due to the porous layer effects on the isotherm distribution along the wall which stems from the dominant of the conductive heat transfer (see Figures 9(d-f)). However, it is nteresting to note that Nu_r in case 2 has a greater value than for case 1.This may be attributed to the main cell in case 2 having a greater elongation along the right-hand cold wall and greater penetration into the porous layer than for case 1. In addition, due to the horizontal arrangement of the porous layer under the nanofluid layer, convective heat transfer is still dominant in the nanofluid layer, with greater penetration through the porous layer for different K_r values compared to case 1. This due to the heat received from the heat source for case 2 is augmented over that in case 1.

4.5 Overall heat transfer and average Nu_{av}

Figures 13a and b show the variation of the average Nusselt number Nu_{av} versus Ra along the left-hand heated sidewall for different values of S and K_r, respectively. The upper and lower panels of the plots represent case 1 and case 2, respectively. It seems that Nu_{av} increases as a logarithmic function of Ra regardless of other parameters. Figure 13a shows the relationship between Nu_{av} and Ra for various S values as Da = 10^{-5}, ϕ = 0.1 and K_r = 1. Increasing S causes Nu_{av} to decrease with Ra. This is because at higher values of S, the resistance area of the porous matrix increases, which leads to the suppression of the convective

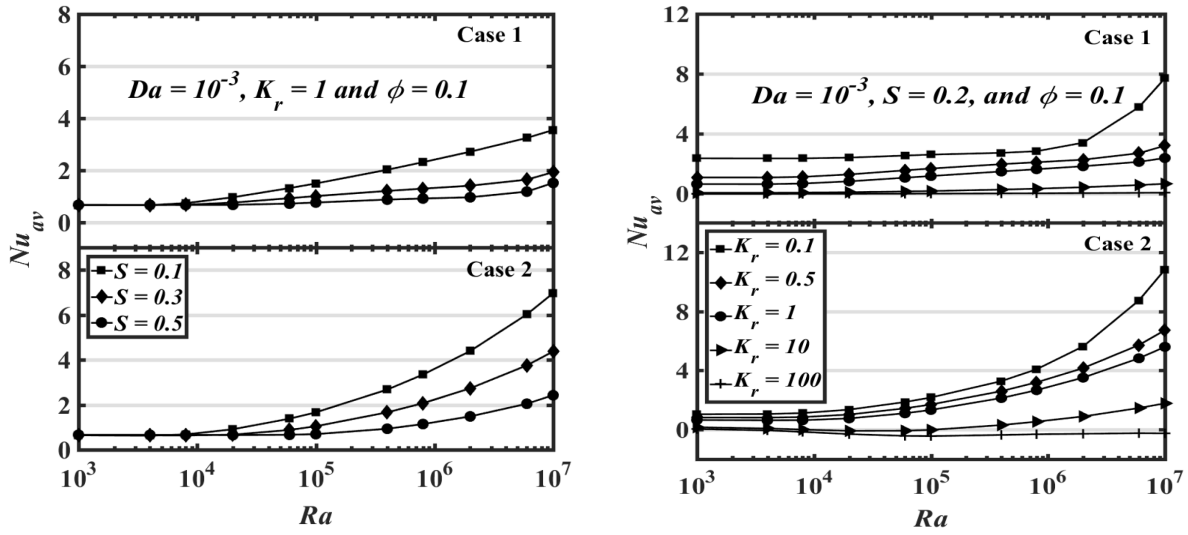

(a) **(b)**

Figure 13: Variation of the average Nusselt number versus *Ra*, **(a)** *S* effect and **(b)** K_r effect. In each plot, the upper panel corresponds to case 1, and the lower panel corresponds to case 2.

heat transfer mode within the porous layer compared to the nanofluid layer. The heat transfer rates appear to take constant values at $Ra \leq 10^4$ due to dominant effect of the conductive heat transfer regardless of the porous layer thickness, implying there is no effect of the porous layer thickness for values of Ra up to 10^4. At constant value of S, it is interesting to note that Nu_{av} increases in a more monotonic manner for case 2 than case 1, indicating that the heat transfer rate for case 2 is greater than for case 1. This stems from the fact that the higher intensity of the streamlines and denser isotherms along the vertical walls with a wide spot of the isotherm lines at the upper region of the cavity, as shown in Figures 8(a-c) and 6(a-c), respectively.

Figure 13b shows the variation of heat transfer rates versus *Ra* along the left-hand heated wall as $Da = 10^{-5}$, $S = 0.2$, and $\phi = 0.1$ for different K_r values. It seems that there is no significant effect of increasing K_r on the rate of heat transfer when $K_r > 1$ and at a low Darcy number, $Da = 10^{-5}$. This indicates that the lower value of Da produces considerable resistance to any natural convection, despite the higher value of $Ra = 10^7$. However, in the nanofluid layer, increasing K_r causes the convective heat transfer to increase monotonically with Ra. At

$Ra = 10^7$, significant increases in Nu_{av} for all values of K_r were found in case 2 compared to case 1, signifying the importance of the porous-nanofluid layer arrangement in the vertical or horizontal direction to heat transfer enhancement inside the cavity.

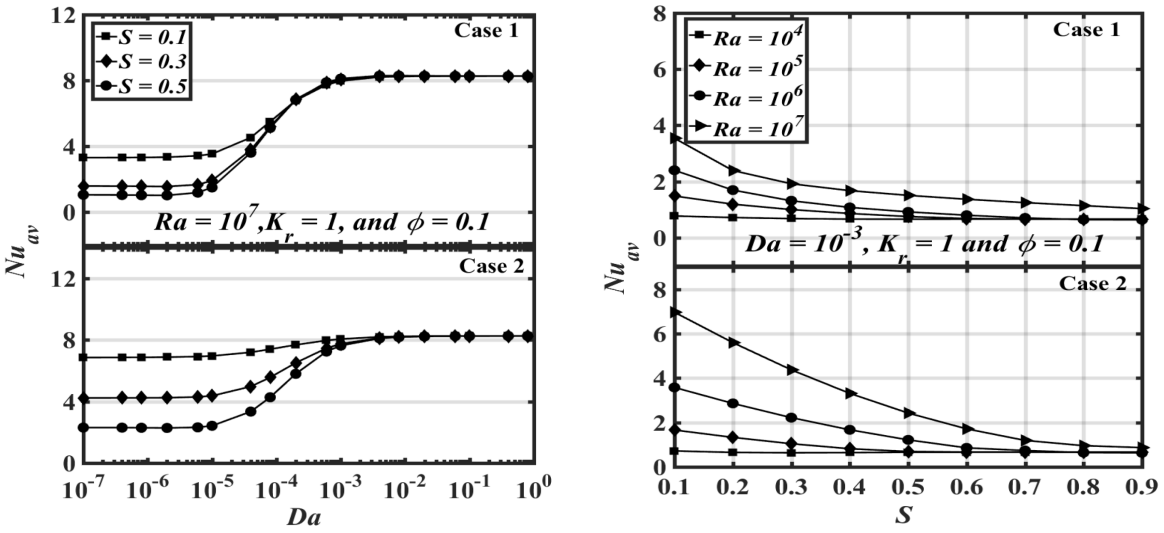

(a) **(b)**

Figure 14: Variation of the average Nusselt number with **(a)** *Da* number for different *S* and with **(b)** porous layer thickness *S* for different *Ra*. In each plot, The upper panel corresponds to case 1, and the lower panel corresponds to case 2.

Figures 14a and b depict the rate of heat transfer versus the Darcy number and porous layer thickness, respectively, along the left-hand heated wall with different parameter values for case 1 (upper panel) and case 2 (lower panel). Examination of the different values of porous layer thickness S on the average Nusselt number versus Da as ϕ = 0.1 and K_r = 1 is illustrated in Figure 14a. For case 1 (upper panel), at the higher value of Ra used in the current study (Ra=10^7) the effect of the porous layer's thickness vanishes at $Da > 10^{-3}$, signifying that the porous layer behaves as a nanofluid layer, and that the porous matrix essentially has no effect in the cavity. Nu_{av} decreases suddenly with decreasing Da values from $Da = 10^{-3}$ to 10^{-5} due to the decrease in permeability of the porous layer, though this decline is significantly reduced when S = 0.1. This is because the porous layer thickness causes an increase in the resistance area produced by the porous layer itself. At values of $Da < 10^{-5}$, Da has no effect on heat

transfer rate for each value of S. For case 2 (lower panel of Figure 14a), it is interesting to observe that Nu_{av} at $Da = 10^{-3}$ for case 1 is higher than case 2 for all values of S. Conversely, at $Da > 10^{-3}$, there is a differential decrease of Nu_{av} with more effect of changing S values compared to case 1 at $10^{-5} \leq Da \leq 10^{-3}$. This pattern causes Nu_{av} to show a greater enhancement of heat transfer for case 2 than case 1, especially at low Darcy numbers, $Da < 10^{-3}$, for each value of S, indicating the effect of the porous-nanofluid layer direction.

Plots of the average Nusselt number versus S are used to illustrate the effect of various values of Ra on the heat transfer rate, as shown in Figure 14b. The upper and lower panels represent case 1 and case 2, respectively. Figure 14b illustrates the effect of Ra for $Da = 10^{-5}$, $\phi = 0.1$ and $K_r = 1$ for case 1 (see the upper panel). As expected, a higher Ra results in higher rate of heat transfer. For a given Ra, the fluid flow resistance increases with increasing S, which leads to reduced convection and results in a lower value of Nu_{av}. For $Ra = 10^5$, the convective heat transfer mode is almost entirely suppressed when $S \geq 0.6$, while there is no effect of S at $Ra = 10^4$. In case 2 (see the lower panel of Figure 14b), the enhancement in heat transfer rate is more pronounced for case 2 compared to case 1, especially at $S = 0.1$ for different values of Ra .

Figure 15 illustrates the variation of average Nusselt number along the left-hand heated wall with logarithmic values of (a) Rayleigh number and (b) Darcy number for case 1 and case 2 when $Da = 10^{-3}$, $S = 0.2$, $\phi = 0.1$, and $K_r = 0.1$. Nu_{av} increases with increasing Ra in both cases, as shown in Figure 15a. A slight change occurs for the linear heating for both cases, where it behaves in a changeable manner with Ra. At $Ra > 10^6$ and $Ra < 10^4$, Nu_{av}values for case 1 are greater than in case 2, while the opposite behaviour is seen for $10^4 \leq Ra \leq 10^6$. Figure 15b illustrates the variation of heat transfer rate with Da as $Ra = 10^6$, $S = 0.2$, $\phi = 0.1$,

and K_r = 0.1 for case 1 and 2. At $Da > 10^{-3}$, Nu_{av} for case 1 is greater than for case 2, whereas the opposite pattern, with relatively higher changes

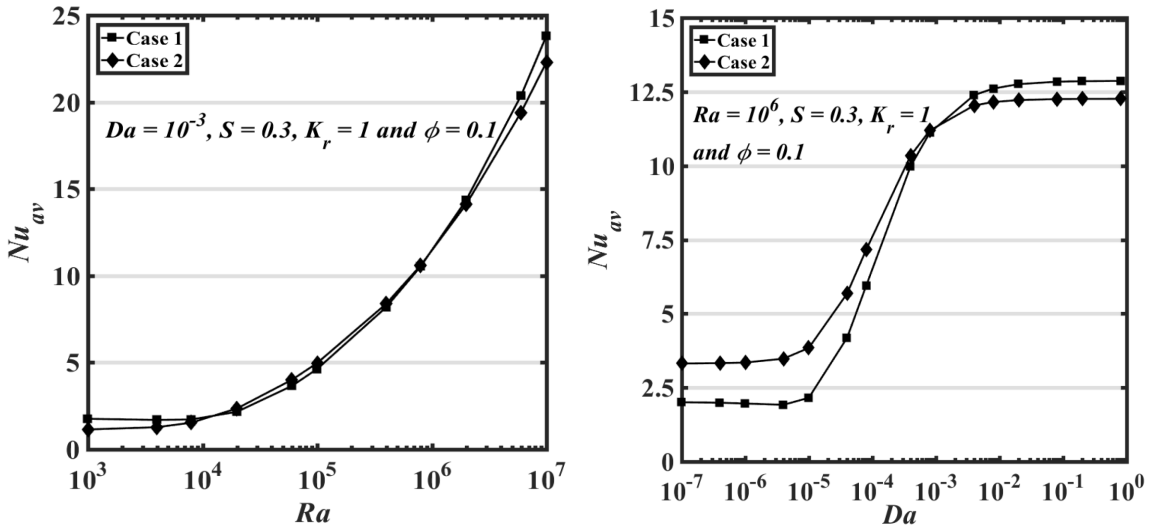

(a) **(b)**

Figure 15: Variation of the average Nusselt number with **(a)** Ra, and **(b)** Da, for case 1 (blue line) and case 2 (black line) with linear heating on the left vertical sidewall.

to the Nusselt number is apparent when $Da < 10^{-3}$. In general, at low values of Da, Nu_{av} for case 2 is greater than for case 1, while the opposite is seen at higher values of Da.

5 Conclusion

The current study analyses the details of fluid flow and heat transfer due to natural convection within square enclosures for two cases depending on the alignment of the porous-nanofluid layers. Case 1 corresponds to the vertical direction, while case 2 corresponds to the horizontal direction. In case 1, the porous layer is positioned on the left of the enclosure while it is located at the bottom of the enclosure for case 2. In both cases, linear heated boundary conditions are applied to the left vertical wall of the cavity while the right vertical wall is isothermally cooled; the horizontal walls are kept insulated. The nanofluid is assumed a pure fluid (water) with Cu nanoparticles, forming a homogeneous mixture. The interaction between the nanofluid layer and porous layer is taken to be permeable. The Galerkin finite element method has been used and smooth results have been obtained in terms of streamlines, isotherms

and heat transfer over wide ranges of the governing parameters such as Ra ($10^3 \leq Ra \leq 10^7$), Da ($10^{-7} \leq Da \leq 1$), S ($0.1 \leq S \leq 0.9$), K_r ($0.1 \leq K_r \leq 100$) and $\phi = 0.1$. Some of the important conclusions can be summarised as follows:

- Due to the linearly heated left-hand wall and the cold right-hand wall of the cavity, two circulating regions were observed, where the main cell moved in the clockwise direction, covering most of the cavity area, while there was also a secondary cell moving in the anticlockwise manner in the upper left corner of the cavity.
- In case 1, increasing the porous layer thickness S produced an increase in flow resistance, which caused a reduction in the rate of heat removal from the left-hand heated wall, especially at low values of Da.
- Increasing Ra caused the intensity of the streamlines in case 2 to be stronger than in case 1.
- Lower values of the thermal conductivity ratio imply greater heat transfer enhancement than for high thermal conductivity ratios.
- The variation of the rate of heat transfer with Ra showed that when $Da = 10^{-3}$, $S = 0.2$, $\phi = 0.1$, and $K_r = 0.1$ at $Ra > 10^6$ and $Ra < 10^4$, Nu_{av}values for case 1 were greater than for case 2, though the opposite behaviour was observed for $10^4 \leq Ra \leq 10^6$, indicative of the importance of the alignment of the porous-nanofluid layers in either the vertical or horizontal direction.
- At the low value of K_r, Nu_{av} was more enhanced for case 2 compared to case 1, especially at the low values of Darcy number $Da < 10^{-3}$ whereas the opposite behaviour of Nu_{av} was observed for high values of Da. This indicates to the importance of the alignment of the porous-nanofluid layers in eithewr the vertical or the horizontal directions.

References

[1] F. Arpino, N. Massarotti, A. Mauro, Efficient three-dimensional FEM based algorithm for the solution of convection in partly porous domains, International Journal of Heat and Mass Transfer, 54(21) (2011) 4495-4506.

[2] M.A. Ismael, A.J. Chamkha, Conjugate natural convection in a differentially heated composite enclosure filled with a nanofluid, Journal of Porous Media, 18(7) (2015).

[3] S. Sathe, W.-Q. Lin, T. Tong, Natural convection in enclosures containing an insulation with a permeable fluid-porous interface, International journal of heat and fluid flow, 9(4) (1988) 389-395.

[4] M. Safaei, M. Goodarzi, M. Mohammadi, Numerical modeling of turbulence mixed convection heat transfer in air filled enclosures by finite volume method, The International Journal of Multiphysics, 5(4) (2016).

[5] M.R. Safaei, B. Rahmanian, M. Goodarzi, Numerical study of laminar mixed convection heat transfer of power-law non-Newtonian fluids in square enclosures by finite volume method, International Journal of Physical Sciences, 6(33) (2011) 7456-7470.

[6] M.R. Safaei, H.R. Goshayeshi, B.S. Razavi, M. Goodarzi, Numerical investigation of laminar and turbulent mixed convection in a shallow water-filled enclosure by various turbulence methods, Scientific Research and Essays, 6(22) (2011) 4826-4838.

[7] M. Afrand, Using a magnetic field to reduce natural convection in a vertical cylindrical annulus, International Journal of Thermal Sciences, 118 (2017) 12-23.

[8] M. Afrand, S. Rostami, M. Akbari, S. Wongwises, M.H. Esfe, A. Karimipour, Effect of induced electric field on magneto-natural convection in a vertical cylindrical annulus filled with liquid potassium, International Journal of Heat and Mass Transfer, 90 (2015) 418-426.

[9] M. Afrand, S. Farahat, A.H. Nezhad, G. Ali Sheikhzadeh, F. Sarhaddi, 3-D numerical investigation of natural convection in a tilted cylindrical annulus containing molten potassium

and controlling it using various magnetic fields, International Journal of Applied Electromagnetics and Mechanics, 46(4) (2014) 809-821.

[10] M. Afrand, S. Farahat, A.H. Nezhad, G.A. Sheikhzadeh, F. Sarhaddi, Numerical simulation of electrically conducting fluid flow and free convective heat transfer in an annulus on applying a magnetic field, Heat Transfer Research, 45(8) (2014).

[11] M. Zadhoush, A.A. Nadooshan, M. Afrand, Constructal optimization of longitudinal and latitudinal rectangular fins used for cooling a plate under free convection by the intersection of asymptotes method, International Journal of Heat and Mass Transfer, 112 (2017) 441-453.

[12] R.R.S. Gorla, A.J. Chamkha, A.M. Rashad, Mixed convective boundary layer flow over a vertical wedge embedded in a porous medium saturated with a nanofluid: natural convection dominated regime, Nanoscale research letters, 6(1) (2011) 1-9.

[13] H. Saleh, R. Roslan, I. Hashim, Natural convection heat transfer in a nanofluid-filled trapezoidal enclosure, International Journal of Heat and Mass Transfer, 54(1) (2011) 194-201.

[14] T. Basak, A.J. Chamkha, Heatline analysis on natural convection for nanofluids confined within square cavities with various thermal boundary conditions, International Journal of Heat and Mass Transfer, 55(21) (2012) 5526-5543.

[15] F. Selimefendigil, H.F. Öztop, A.J. Chamkha, MHD mixed convection and entropy generation of nanofluid filled lid driven cavity under the influence of inclined magnetic fields imposed to its upper and lower diagonal triangular domains, Journal of Magnetism and Magnetic Materials, (2016).

[16] S.S. Rao, A. Srivastava, Interferometric study of natural convection in a differentially-heated cavity with Al 2 O 3–water based dilute nanofluids, International Journal of Heat and Mass Transfer, 92 (2016) 1128-1142.

[17] I. Hashim, A. Alsabery, Conjugate Free Convection in a Square Cavity Filled with Nanofluid and Heated from Below by Spatial Wall Temperature, World Academy of Science,

Engineering and Technology, International Journal of Mechanical, Aerospace, Industrial, Mechatronic and Manufacturing Engineering, 10(4) (2016) 687-690.

[18] M. Goodarzi, M. Safaei, K. Vafai, G. Ahmadi, M. Dahari, S. Kazi, N. Jomhari, Investigation of nanofluid mixed convection in a shallow cavity using a two-phase mixture model, International Journal of Thermal Sciences, 75 (2014) 204-220.

[19] F. Garoosi, M.R. Safaei, M. Dahari, K. Hooman, Eulerian–Lagrangian analysis of solid particle distribution in an internally heated and cooled air-filled cavity, Applied Mathematics and Computation, 250 (2015) 28-46.

[20] M. Afrand, A.A. Nadooshan, M. Hassani, H. Yarmand, M. Dahari, Predicting the viscosity of multi-walled carbon nanotubes/water nanofluid by developing an optimal artificial neural network based on experimental data, International Communications in Heat and Mass Transfer, 77 (2016) 49-53.

[21] M.R. Safaei, A. Jahanbin, A. Kianifar, S. Gharehkhani, A.S. Kherbeet, M. Goodarzi, M. Dahari, Mathematical modeling for nanofluids simulation: a review of the latest works, in: Modeling and Simulation in Engineering Sciences, InTech, 2016.

[22] M.R. Safaei, M. Safdari Shadloo, M.S. Goodarzi, A. Hadjadj, H.R. Goshayeshi, M. Afrand, S. Kazi, A survey on experimental and numerical studies of convection heat transfer of nanofluids inside closed conduits, Advances in Mechanical Engineering, 8(10) (2016) 1687814016673569.

[23] O.A. Akbari, M.R. Safaei, M. Goodarzi, N.S. Akbar, M. Zarringhalam, G.A.S. Shabani, M. Dahari, A modified two-phase mixture model of nanofluid flow and heat transfer in a 3-D curved microtube, Advanced Powder Technology, 27(5) (2016) 2175-2185.

[24] M. Afrand, Experimental study on thermal conductivity of ethylene glycol containing hybrid nano-additives and development of a new correlation, Applied Thermal Engineering, 110 (2017) 1111-1119.

[25] A. Karimi, M. Afrand, Numerical study on thermal performance of an air-cooled heat exchanger: Effects of hybrid nanofluid, pipe arrangement and cross section, Energy Conversion and Management, 164 (2018) 615-628.

[26] M.H. Bahmani, G. Sheikhzadeh, M. Zarringhalam, O.A. Akbari, A.A. Alrashed, G.A.S. Shabani, M. Goodarzi, Investigation of turbulent heat transfer and nanofluid flow in a double pipe heat exchanger, Advanced Powder Technology, (2017).

[27] A.A. Hassan, M.A. Ismael, Mixed Convection in Superposed Nanofluid and Porous Layers Inside Lid-Driven Square Cavity, Int. J. of Thermal & Environmental Engineering, 10(2) (2015) 93-104.

[28] M.T. Nguyen, A.M. Aly, S.-W. Lee, Natural convection in a non-darcy porous cavity filled with cu–water nanofluid using the characteristic-based split procedure in finite-element method, Numerical Heat Transfer, Part A: Applications, 67(2) (2015) 224-247.

[29] A.J. Chamkha, M.A. Ismael, Natural convection in differentially heated partially porous layered cavities filled with a nanofluid, Numerical Heat Transfer, Part A: Applications, 65(11) (2014) 1089-1113.

[30] A. Alsabery, A. Chamkha, S. Hussain, H. Saleh, I. Hashim, Heatline visualization of natural convection in a trapezoidal cavity partly filled with nanofluid porous layer and partly with non-Newtonian fluid layer, Advanced Powder Technology, 26(4) (2015) 1230-1244.

[31] H.F. Oztop, M. Mobedi, E. Abu-Nada, I. Pop, A heatline analysis of natural convection in a square inclined enclosure filled with a CuO nanofluid under non-uniform wall heating condition, International Journal of Heat and Mass Transfer, 55(19) (2012) 5076-5086.

[32] H.T. Cheong, H.T. Cheong, S. Sivasankaran, S. Sivasankaran, M. Bhuvaneswari, M. Bhuvaneswari, Natural convection in a wavy porous cavity with sinusoidal heating and internal heat generation, International Journal of Numerical Methods for Heat & Fluid Flow, 27(2) (2017) 287-309.

[33] S. Sivasankaran, M. Bhuvaneswari, Natural convection in a porous cavity with sinusoidal heating on both sidewalls, Numerical Heat Transfer, Part A: Applications, 63(1) (2013) 14-30.

[34] M. Bhuvaneswari, S. Sivasankaran, Y. Kim, Magnetoconvection in a square enclosure with sinusoidal temperature distributions on both side walls, Numerical Heat Transfer, Part A: Applications, 59(3) (2011) 167-184.

[35] M. Sathiyamoorthy, A. Chamkha, Effect of magnetic field on natural convection flow in a liquid gallium filled square cavity for linearly heated side wall (s), International Journal of Thermal Sciences, 49(9) (2010) 1856-1865.

[36] M. Sathiyamoorthy, A.J. Chamkha, Natural convection flow under magnetic field in a square cavity for uniformly (or) linearly heated adjacent walls, International Journal of Numerical Methods for Heat & Fluid Flow, 22(5) (2012) 677-698.

[37] A.J. Chamkha, M. Abd El-Aziz, S.E. Ahmed, Hydromagnetic double-diffusive convection in a rectangular enclosure with linearly heated and concentrated wall (s) in the presence of heat generation/absorption effects, Progress in Computational Fluid Dynamics, an International Journal, 12(6) (2012) 400-414.

[38] M. Sathiyamoorthy, A. J. Chamkha, Analysis of natural convection in a square cavity with a thin partition for linearly heated side walls, International Journal of Numerical Methods for Heat & Fluid Flow, 24(5) (2014) 1057-1072.

[39] T. Basak, S. Roy, A. Matta, I. Pop, Analysis of heatlines for natural convection within porous trapezoidal enclosures: effect of uniform and non-uniform heating of bottom wall, International Journal of Heat and Mass Transfer, 53(25) (2010) 5947-5961.

[40] T. Basak, P.K. Pradeep, S. Roy, I. Pop, Finite element based heatline approach to study mixed convection in a porous square cavity with various wall thermal boundary conditions, International Journal of Heat and Mass Transfer, 54(9) (2011) 1706-1727.

[41] M. Sathiyamoorthy, T. Basak, S. Roy, I. Pop, Steady natural convection flow in a square cavity filled with a porous medium for linearly heated side wall (s), International Journal of Heat and Mass Transfer, 50(9) (2007) 1892-1901.

[42] F. Wu, W. Zhou, X. Ma, Natural convection in a porous rectangular enclosure with sinusoidal temperature distributions on both side walls using a thermal non-equilibrium model, International Journal of Heat and Mass Transfer, 85 (2015) 756-771.

[43] S. Sivasankaran, A. Malleswaran, J. Lee, P. Sundar, Hydro-magnetic combined convection in a lid-driven cavity with sinusoidal boundary conditions on both sidewalls, International Journal of Heat and Mass Transfer, 54(1) (2011) 512-525.

[44] G.R. Kefayati, Lattice Boltzmann simulation of MHD natural convection in a nanofluid-filled cavity with sinusoidal temperature distribution, Powder technology, 243 (2013) 171-183.

[45] H.M. Elshehabey, S.E. Ahmed, MHD mixed convection in a lid-driven cavity filled by a nanofluid with sinusoidal temperature distribution on the both vertical walls using Buongiorno's nanofluid model, International Journal of Heat and Mass Transfer, 88 (2015) 181-202.

[46] A.H. Pordanjani, A. Jahanbakhshi, A.A. Nadooshan, M. Afrand, Effect of two isothermal obstacles on the natural convection of nanofluid in the presence of magnetic field inside an enclosure with sinusoidal wall temperature distribution, International Journal of Heat and Mass Transfer, 121 (2018) 565-578.

[47] A. Mahmoudi, I. Mejri, M.A. Abbassi, A. Omri, Lattice Boltzmann simulation of MHD natural convection in a nanofluid-filled cavity with linear temperature distribution, Powder Technology, 256 (2014) 257-271.

[48] H.F. Oztop, E. Abu-Nada, Y. Varol, K. Al-Salem, Computational analysis of non-isothermal temperature distribution on natural convection in nanofluid filled enclosures, Superlattices and Microstructures, 49(4) (2011) 453-467.

[49] A. Alsabery, A. Chamkha, H. Saleh, I. Hashim, Heatline visualization of conjugate natural convection in a square cavity filled with nanofluid with sinusoidal temperature variations on both horizontal walls, International Journal of Heat and Mass Transfer, 100 (2016) 835-850.

[50] G. Bourantas, E. Skouras, V. Loukopoulos, V. Burganos, Heat transfer and natural convection of nanofluids in porous media, European Journal of Mechanics-B/Fluids, 43 (2014) 45-56.

[51] M.A. Sheremet, I. Pop, Natural convection in a wavy porous cavity with sinusoidal temperature distributions on both side walls filled with a nanofluid: Buongiorno's mathematical model, Journal of Heat Transfer, 137(7) (2015) 072601.

[52] A. Alsabery, A. Chamkha, H. Saleh, I. Hashim, Natural Convection Flow of a Nanofluid in an Inclined Square Enclosure Partially Filled with a Porous Medium, Scientific Reports, 7 (2017).

[53] R. Nasrin, S. Parvin, Investigation of buoyancy-driven flow and heat transfer in a trapezoidal cavity filled with water–Cu nanofluid, International Communications in Heat and Mass Transfer, 39(2) (2012) 270-274.

[54] S. Patankar, Numerical heat transfer and fluid flow, CRC press, 1980.

[55] T. Basak, S. Roy, H.S. Takhar, Effects of nonuniformly heated wall (s) on a natural-convection flow in a square cavity filled with a porous medium, Numerical Heat Transfer, Part A: Applications, 51(10) (2007) 959-978.

[56] C. Beckermann, S. Ramadhyani, R. Viskanta, Natural convection flow and heat transfer between a fluid layer and a porous layer inside a rectangular enclosure, Journal of heat transfer, 109(2) (1987) 363-370.